J. Fluid Mech. (2003), *vol.* 496, *pp.* 73–103.
DOI: 10.1017/S0022112003006487 Printed in the United Kingdom

Quasi-equilibrium dynamics of shear-stratified turbulence in a model tropospheric jet

By K. L. TSE, A. MAHALOV, B. NICOLAENKO AND H. J. S. FERNANDO

Environmental Fluid Dynamics Program, Arizona State University, Tempe, AZ 85287-9809, USA

(Received 17 September 2001 and in revised form 17 June 2003)

Direct numerical simulations are performed to study the dynamics of an inhomogeneous stratified shear flow that models an atmospheric jet centred at the tropopause across which the density stratification is non-uniform. Small to moderate background stratifications are selected, and simulations are conducted for a range of Reynolds and Froude numbers. A spectral domain decomposition method that is particularly suitable for simulations of non-uniformly stratified shear flows is developed to simulate the desired turbulent jet, and quasi-equilibrium flow fields are obtained by long-time integration of governing equations. The structures of the mean flow and turbulence fields are calculated, which are interpreted using relevant length scales (Ozmidov, buoyancy, shear, Ellison) and Richardson number profiles. The ratios of the Ellison to buoyancy scales are much smaller than unity at the jet core and approach unity at the edges, confirming that mechanical turbulence prevails in the jet core, while nonlinear waves and stratification effects are dominating at the jet edges. The jet core is found to support sustained mechanical (active) turbulence, outside which lay a region of patchy turbulence and nonlinear gravity wave activity characterized by spatially decaying velocity fluctuations and strong temperature fluctuations. Detailed energy budgets show how energy is partitioned within the flow, including the transport of energy from the jet to its immediate vicinity by nonlinear gravity waves.

1. Introduction

In environmental flows situations where shear and stratification coexist are ubiquitous, and many attempts have been made to understand the generation and evolution of turbulence in stratified shear flows. In particular, it has long been recognized that shear is a major source of mixing in geophysical flows, in that it not only produces turbulence via interaction with Reynolds stresses but also directly causes mixing at stratified interfaces by exciting Kelvin–Helmholtz (K–H) instabilities. The effect of stable stratification is to limit the vertical length scales of the turbulence and hence the vertical length scales over which mixing can occur. The usual feature of unstratified turbulence of having a single or a few length scales is not a characteristic of stratified turbulence, especially when the shear and buoyancy forcing have different length scales and when there is significant wave dynamics.

Early studies of shear-stratified turbulence have been made using laboratory simulations (Webster 1964; Rohr *et al.* 1988), but with increasing computer power, direct numerical simulations (DNS) and large-eddy simulations (LES) have become viable tools. There are many studies using numerical approaches, most of them using

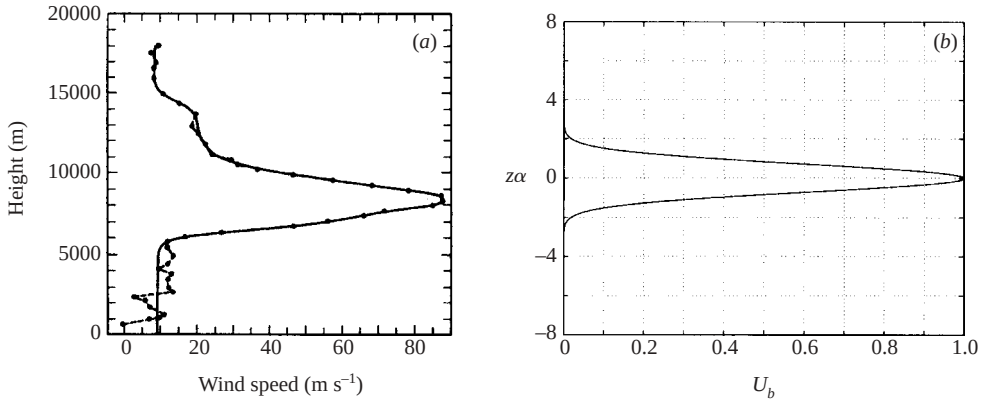

FIGURE 1. (*a*) An example of a jet stream profile from Bedard *et al.* (1986) (reproduced with permission from the American Meteorological Society). The dotted line is obtained from observation while the solid line is a numerical fit. (*b*) The normalized velocity profiles U_b for the basic state of the present computations. The vertical axis is $z\alpha$ where $\alpha = 16$, and $-8.0 \leqslant z\alpha \leqslant 8.0$. Only the middle portion of the computational box is shown here.

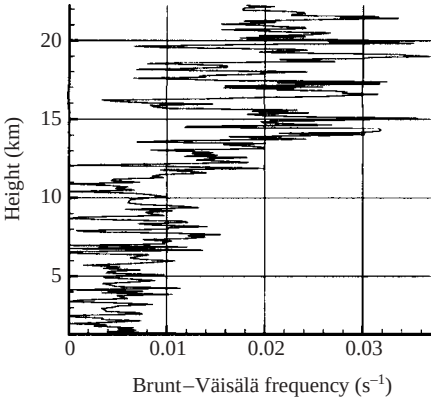

FIGURE 2. Brunt–Väisälä frequency profile recorded in the atmosphere by Beland (1993) with balloon measurements.

DNS (Gerz, Schumann & Elghobashi 1989; Holt, Koseff & Ferziger 1992; Schumann & Gerz 1995; Hunt & Galmiche 2001; Galmiche, Thual & Bonneton 2002; Jacobitz, Sarkar & Van Atta 1997; Riley, Metcalfe & Weissman 1981; Shih *et al.* 2000; Riley 2001) and others using LES (Kaltenbach, Gerz & Schumann 1994; Schumann 1996; Carnevale, Briscoline & Orlandi 2001). There are also many investigations based on observational data, e.g. Keyser & Shapiro 1985; Bedard, Canavero & Einaudi 1986; Hunt, Kaimal & Gaynor 1985; Nastrom & Gage 1985; Nastrom, Gage & Ecklund 1986; Eaton & Nastrom 1998, Pardyjak, Monti & Fernando 2002.

The focus of the present study is to investigate turbulence in a non-homogeneous stratified shear flow where the velocity profile takes the form of a jet (cf. figure 1). In the upper troposphere and lower stratosphere localized regions of three-dimensional turbulence arise through shear instability or through breaking of inertia–gravity waves. Upper-level atmospheric jet regions are also strongly influenced by stable background stratification (cf. figure 2). The flow belongs to the class of non-uniformly stratified (with a doubling of buoyancy frequency across the jet) shear flows, whose turbulence

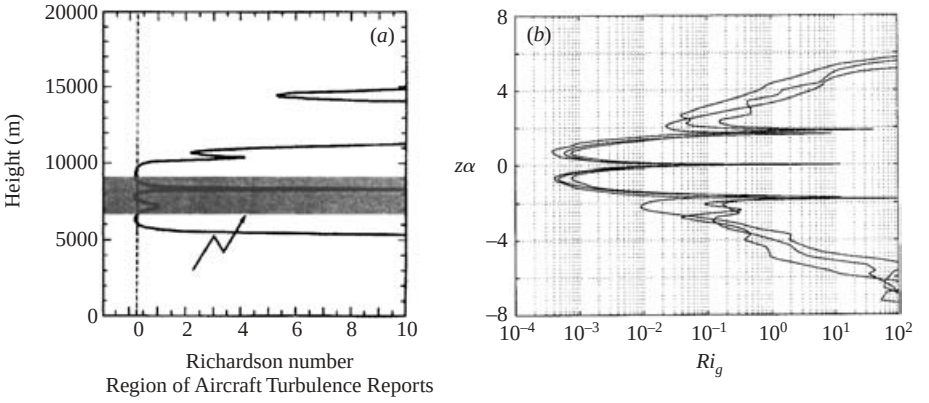

FIGURE 3. (*a*) An example of a gradient Richardson number profile corresponding to figure 1(*a*), measured by Bedard *et al.* (1986) (reproduced with permission from the American Meteorological Society). (*b*) Gradient Richardson number profiles at quasi-equilibrium from the numerical simulations for cases 4, 5 ($256^2 \times 512$ resolution) and case 6 ($512^2 \times 1024$ resolution) (see table 1).

characteristics are not well-understood. We set up our model based on jet streams encountered in the Earth's atmosphere at the tropopause. This region corresponds to the transition between the troposphere and the stratosphere which is observed at an altitude of about 10 to 15 km depending on the latitude. We consider a non-uniformly stratified jet centred at the vertical coordinate $z = 0$. The flow consists of a jet core surrounded by two shear layers; the layer above has a negative shear and a stronger temperature gradient, while the layer below has a positive shear and presents a weaker temperature gradient, with the buoyancy (Brunt–Väisälä) frequency being reduced by a factor of two. This configuration is typical of the jet streams in the tropopause (cf. figures 1 and 2).

The gradient Richardson number, which quantifies the ratio of stratification to shear effects, is low within the jet core (except at the centre) and velocity fluctuations are maximal there, thus providing sustained turbulence (cf. figures 3*a* and 3*b*). It increases towards the jet edges where the effect of stratification tends to reduce turbulence with the shear length scale exceeding the buoyancy outer scale. Tropopausal turbulence, driven by shear instabilities on either side of the jet axis, results in mean stratification with a notch in the Brunt–Väisälä frequency profile, a configuration favouring gravity wave emission (Nastrom & Eaton 1997). The flow in the vicinity of the edges of the jet produces nonlinear gravity waves, which travel into the ambient stratification and break (Sutherland & Peltier 1995). Regions far from the jet edges have weaker velocity fluctuations than in the core, and hence meagre turbulent mixing, although potential energy and temperature fluctuations therein remain strong due to internal waves. The above scenarios are in agreement with aircraft observations of Bedard *et al.* (1986). The regions of intermittent turbulence are signified by low values of gradient Richardson number Ri_g, typically $Ri_g < 0.25$ (Kaltenbach *et al.* 1994).

In this study, our focus is on the dynamics and vertical variability of scales that are poorly resolved in mesoscale meteorological codes such as MM5 and WRF (Grell, Dudhia & Stauffer 1995). Such knowledge is important not only for parameterization and modelling of tropopausal turbulence and associated mixing in mesoscale models under stably stratified conditions, but also for determining refractive index structure functions pertinent to electromagnetic wave propagation across the tropopause

(Beland 1993; Eaton & Nastrom 1998; Nastrom *et al.* 1986; Dalaudier *et al.* 1994). Vertical scales controlling the size of 'sheets' in the atmospheric temperature field have been directly found by the analysis of field measurements; the main dynamical properties of such layers, whether strongly mixed or 'calm', can be characterized by the gradient Richardson number and various outer scales of turbulence (Alisse & Sidi 2000). We investigate how the dynamics and dominant physical processes in the stratified jet are reflected in various length scales. In particular, we study vertical variability of outer scales and their dependence on the background synoptic-scale jet stream and the background Brunt–Väisälä profile across the tropopause. Beyond a sufficient threshold of resolution (especially in the vertical direction) our DNS simulations demonstrate saturation with increased numerical resolution of the vertical variability curves for ratios of various outer scales of turbulence. These resolution-independent ratios are an effective gauge of the variability of non-homogeneous turbulence in a non-uniformly stratified tropopause jet.

Only a very few studies have been reported on three-dimensional high-resolution numerical simulations that employ realistic models of the non-uniformly stratified tropopause jet. Sutherland & Peltier (1995) and Smyth & Moum (2002) implemented a jet-like velocity profile as the initial condition; the Brunt–Väisälä profiles used in their model were also doubled from the lower to the upper domains. However, their simulations are only two-dimensional and the jet profiles tend to be smeared as there is no sustained momentum source in their model, which caused the shear to steadily decrease. In the atmosphere, on the other hand, the jet is maintained in a quasi-steady state by the synoptic-scale forcing, which needs to be considered in modelling. It should be noted that there are many numerical studies of stratified turbulent shear flows, which impose a constant mean shear and stratification in the vertical direction. The horizontal directions are then regarded as periodic and the vertical direction shear is periodic. The work by Gerz *et al.* (1989), Holt *et al.* (1992), Kaltenbach *et al.* (1994), Carnevale *et al.* (2001) and Jacobitz *et al.* (1997) belong to this category. Turbulent flows with mean shear and stratification are typically temporally evolving and hence do not reach stationary states, except at a certain 'stationary' Richardson number for which the production is balanced by the dissipation. Asymptotic stationary states can be attained, however, where normalized variables (e.g. ratios of individual components of energy to total energy) reach constant values after several turnover periods. Another approach for the study of shear-stratified turbulence uses decaying simulations. An example is the DNS study of Galmiche *et al.* (2002), that deals with non-uniform vertical mean shear and non-uniform stratification, where mean velocity and density profiles are allowed to evolve with time. In such simulations, however, the results are sensitive to the generally transient nature of the flow.

While previous numerical studies have made important contributions to the study of shear-stratified turbulence, they do not reproduce the exact middle atmospheric situation wherein the turbulence can reach some quasi-equilibrium state. Furthermore, if homogeneous boundary conditions are used in the vertical direction, there is no net heat and momentum transfer out of the box. As we demonstrate in § 3, the fluxes play an important role in redistributing energy in the vertical direction. Without such a mechanism, the variability of the atmospheric turbulence around the jet cannot be reproduced. It has been shown in Sutherland & Peltier (1995) that the momentum flux created from the jet produces internal gravity waves which in turn produce a drag on the mean velocity. These phenomena cannot be reproduced by conventional shear periodic numerical experiments, the application of which to atmospheric tropopause simulations in the presence of a jet stream is thus limited.

Another class of closely related problems concerns mixing layers. A large number of studies on mixing layers using theoretical, experimental and numerical approaches have been documented (e.g. Bell & Mehta 1990; Rogers & Moser 1993). Those studies are invaluable in understanding self-similar turbulent statistics as well as the transitional dynamics from the onset of instabilities to full scale turbulence, for example from the formation of K–H billows to pairing of rollers due to subharmonic disturbance, and to the formation of the braid regions and streamwise rib vortices between the rollers, and ensuing mixing in stable environments (Thorpe 1987; Peltier & Caulfield 2003). Most of the studies on mixing layers, however, are limited to the transition period. Even though a self-similar state is usually obtained within a certain time interval, the overall energy budgets are non-stationary at any instance.

Our model of the atmospheric tropopause is characterized by a stratified thin layer across which the buoyancy frequency jumps approximately by a factor of 2 (figure 2). In our three-dimensional DNS, the streamwise velocity that characterizes the basic state of the model jet was given a Gaussian profile, thus producing shear at different vertical levels characteristic of a jet stream. The governing equations are then solved using DNS based on a spectral domain technique developed specifically for flows characterized by non-uniform background shear and stratification (Tse *et al.* 2001). Due to inhomogeneity in the vertical direction, periodic boundary conditions are not used; previous numerical studies have assumed such periodicity. In our simulations, nonlinear shear and stratification profiles adjust to quasi-stationary values, around which the potential and kinetic energies fluctuate. Quasi-equilibrium solutions are obtained following long-time integration of the governing equations. We investigate the effects of inhomogeneity of shear and stratification, especially those properties that are distinct from homogeneous stratified shear flows. The robustness of our results has been verified by DNS with doubled resolution (1024 vertical levels). Thus, the physical results reported here, in particular those involving ratios of outer scales, are independent of the numerical resolution.

The next section describes the computational framework for non-homogeneous stratified shear flows. Section 3 presents the results of numerical simulations and discussions of various mean quantities and variances at quasi-equilibrium. Vertical variability of natural length scales (Ozmidov, buoyancy, shear and Ellison) and Richardson number profiles are analysed in § 4. Turbulent budget equations are investigated in § 5. Conclusions and suggestions for future work are discussed in § 6.

2. Computational framework for non-homogeneous stratified shear flows

2.1. *Description of numerical experiments*

The governing equations are the three-dimensional incompressible Navier–Stokes equations for the velocity $\boldsymbol{U}$ and temperature Θ under the Boussinesq approximation:

$$\frac{\partial U}{\partial t} + \boldsymbol{U}\cdot\nabla U = -\frac{\partial P}{\partial x} + \nu\nabla^2 U + \Pi_U, \tag{2.1}$$

$$\frac{\partial V}{\partial t} + \boldsymbol{U}\cdot\nabla V = -\frac{\partial P}{\partial y} + \nu\nabla^2 V, \tag{2.2}$$

$$\frac{\partial W}{\partial t} + \boldsymbol{U}\cdot\nabla W = -\frac{\partial P}{\partial z} + \nu\nabla^2 W + g\beta(\Theta - \Theta_R), \tag{2.3}$$

$$\frac{\partial \Theta}{\partial t} + \boldsymbol{U}\cdot\nabla\Theta = \kappa\nabla^2\Theta + \Pi_\Theta, \tag{2.4}$$

$$\nabla\cdot\boldsymbol{U} = 0, \tag{2.5}$$

where $\boldsymbol{U}=(U, V, W)$ are the three components of the velocity in the streamwise, spanwise and vertical directions (denoted as x,y,z), respectively; Θ_R is the constant reference temperature; P is the pressure; and ν, κ, β and g are the molecular viscosity, molecular diffusivity, thermal expansion coefficient and gravitational acceleration, respectively. The horizontally homogeneous terms Π_U and Π_Θ are the vertically dependent momentum and thermal sources. The two source terms enable a basic (unstable) jet stream profile and the desired vertically variable Brunt–Väisälä frequency profile to be obtained. They represent large-scale momentum and thermal forcing responsible for maintaining the jet.

In this paper, the total instantaneous variables are represented by upper-case letters (U, V, W, Θ). They are decomposed into two parts: basic state and perturbations. The variables in the basic state are represented by upper-case letters with subscripts (U_b and $\Theta_R+\Theta_b$), and perturbations by lower-case letters (u, v, w, θ). The perturbation is further decomposed into two components: a mean (horizontally averaged) part denoted by $\langle\cdot\rangle$ and a fluctuating component denoted by primes. Thus, the variables U, V, W, Θ are decomposed as

$$U = U_b(z)+u(x, y, z, t)=U_b(z)+\langle u\rangle(z, t)+u'(x, y, z, t), \tag{2.6}$$

$$V = v(x, y, z, t)=\langle v\rangle(z, t)+v'(x, y, z, t), \tag{2.7}$$

$$W = w(x, y, z, t)=w'(x, y, z, t), \tag{2.8}$$

$$\Theta = \Theta_R+\Theta_b(z)+\theta(x, y, z, t)=\Theta_R+\Theta_b(z)+\langle\theta\rangle(z, t)+\theta'(x, y, z, t). \tag{2.9}$$

We have $\langle u'\rangle=\langle v'\rangle=\langle w'\rangle=0$. The mean (horizontally averaged) values of U and Θ contain a part from the basic state and a part from the perturbation (e.g. $\overline{U}=U_b+\langle u\rangle$), while the mean of V satisfies ($\overline{V}=\langle v\rangle$). The pressure can also be decomposed as

$$P = P_b(z)+p(x, y, z, t)=P_b(z)+\langle p\rangle(z, t)+p'(x, y, z, t). \tag{2.10}$$

For the basic state, where the perturbations u, v, w and θ are zero and the fields depend only on z, the governing equations are reduced to

$$\Pi_U+\nu\frac{\partial^2 U_b}{\partial z^2}=0, \tag{2.11}$$

$$\frac{\partial P_b}{\partial z}=g\beta\Theta_b, \qquad \Pi_\Theta=-\kappa\frac{\partial^2\Theta_b}{\partial z^2}. \tag{2.12}$$

Here Π_U is obtained by assigning to U_b the following Gaussian form:

$$U_b(z)=U_b(0)\exp(-(\alpha_1 z)^2)\exp\left(-\left(\frac{L_z}{L_z-z}\right)^2\right)\exp\left(-\left(\frac{L_z}{L_z+z}\right)^2\right)\mathrm{e}^2, \tag{2.13}$$

where α_1 is the stiffness parameter and L_z is the half-depth of the computational box. The velocity profile $U_b(z)$ is equal to $U_b(0)$ at the centre. The momentum source Π_U and the thermal source Π_Θ are obtained from (2.11) and (2.12), respectively. The momentum source is intended to maintain a sustained synoptic/planetary jet stream in the model (figure 1). The thermal source maintains the mesoscale doubling of the buoyancy frequency across the tropopause. Thus, we are resolving a microscale box centred on a synoptic-scale jet stream at the tropopause, for times much shorter than the time scales of mean jet dynamics. The jet profile for U_b is shown in figure 1(b), with $\alpha=\alpha_1=16$. This profile models the measured wind profile of an atmospheric jet shown in figure 1(a).

In (2.12), the buoyancy force due to the background temperature gradient is balanced by the basic-state pressure gradient, and the thermal source is balanced by the diffusion of the background temperature. Substituting (2.9), (2.10) and (2.12) into (2.3)–(2.4), the equations for vertical velocity and temperature can then be expressed as

$$\frac{\partial W}{\partial t} + \boldsymbol{U}\cdot\nabla W = -\frac{\partial p}{\partial z} + g\beta\theta + \nu\nabla^2 W, \tag{2.14}$$

$$\frac{\partial \theta}{\partial t} + \boldsymbol{U}\cdot\nabla\theta = -W\frac{\partial \Theta_b}{\partial z} + \kappa\nabla^2\theta, \tag{2.15}$$

where β is the thermal expansion coefficient. Next, letting $N^2K^2(z) = g\beta\partial\Theta_b(z)/\partial z$ and $\vartheta = g\beta\theta/N$, where N is a constant (N^{-1} has the unit of time) and $K(z)$ is a vertical profile factor we obtain the rescaled vertical velocity and temperature equations (e.g. Herring & Metais 1989)

$$\frac{\partial W}{\partial t} + \boldsymbol{U}\cdot\nabla W = -\frac{\partial p}{\partial z} + N\vartheta + \nu\nabla^2 W, \tag{2.16}$$

$$\frac{\partial \vartheta}{\partial t} + \boldsymbol{U}\cdot\nabla\vartheta = -WNK^2 + \kappa\nabla^2\vartheta. \tag{2.17}$$

The variable ϑ has the unit of length/time (not to be confused with θ, which has the unit of temperature). In the above equation N and $K(z)$ are related to the usual Brunt–Väisälä frequency profile $\mathcal{N}^2(z) = (g/\Theta)(\partial\Theta/\partial z)$ as

$$N^2K^2(z) = g\beta\frac{\partial\Theta_b}{\partial z} = \beta\Theta\mathcal{N}^2(z). \tag{2.18}$$

In our simulations, the non-dimensional $K(z)$ profile has the following form:

$$K(z) = 1 + \frac{1}{\exp(-\alpha_2 z) + 1}. \tag{2.19}$$

The $K(z)$ profile corresponds to a temperature profile which increases monotonically from the bottom to the tropopause level, experiences a stiff transition at the tropopause which depends on the stiffness parameter α_2, and then further increases, reaching at the top twice the value at the bottom. This dimensionless profile models the doubling of the Brunt–Väisälä frequency at the tropopause, as observed in balloon field measurements by Beland (1993), figure 2 (doubling roughly from $0.01\,\mathrm{s}^{-1}$ to $0.02\,\mathrm{s}^{-1}$). Equations (2.13) and (2.19) introduce two parameters α_1 and α_2, which specify the inverse of the external length scales of the system. The first number α_1 controls the amount of shear along the jet edges while the second parameter α_2 controls the stiffness in the Brunt–Väisälä profile. In our simulations, the same values are used for α_1 and α_2 ($\alpha = \alpha_1 = \alpha_2 = 16$). The edges of the jet are then located in the vicinity of the normalized vertical levels $z\alpha \approx \pm 1$.

The variables can be non-dimensionalized by choosing a suitable velocity scale $U_\alpha = U_b(0)$ and length scale L_α. We define $L_\alpha = 1/\alpha$ and $\tilde{z} = \alpha z = z/L_\alpha$. Hence, in terms of the rescaled $\tilde{z}$ and with $\alpha = 16$, the computational box corresponds to $-5.0\times 16 \leqslant \tilde{z} \leqslant 5.0\times 16$. Similarly, we rescale $\tilde{x} = \alpha x$, $\tilde{y} = \alpha y$, with $0 \leqslant \tilde{x}, \tilde{y} \leqslant 8\pi$. The non-dimensionalized equations then become

$$\frac{\partial \tilde{U}}{\partial \tilde{t}} + \tilde{\boldsymbol{U}}\cdot\tilde{\nabla}\tilde{U} = -\frac{\partial \tilde{P}}{\partial \tilde{x}} + \frac{1}{Re_0}\tilde{\nabla}^2\tilde{U} + \tilde{\Pi}_U, \tag{2.20}$$

$$\frac{\partial \tilde{V}}{\partial \tilde{t}} + \tilde{\boldsymbol{U}}\cdot\tilde{\nabla}\tilde{V} = -\frac{\partial \tilde{P}}{\partial \tilde{y}} + \frac{1}{Re_0}\tilde{\nabla}^2\tilde{V}, \tag{2.21}$$

Case	$U_b(0)$	Resolution	$Re_0 = U_b/\nu\alpha$	N
1	4	$128^2 \times 512$	2500	0.2
2	4	$128^2 \times 512$	2500	1.0
3	4	$128^2 \times 512$	2500	0.05
4	10	$256^2 \times 512$	6250	0.2
5	20	$256^2 \times 512$	12500	0.2
6	20	$512^2 \times 1024$	20833	0.2

TABLE 1. Physical parameters used in simulations with $\nu = 1 \times 10^{-4}$, $\kappa = 1.4 \times 10^{-4}$ (cases 1–5) and $\nu = 6 \times 10^{-5}$, $\kappa = 8.6 \times 10^{-5}$ (case 6). $Pr = 0.7$ in all cases.

$$\frac{\partial \tilde{W}}{\partial \tilde{t}} + \tilde{\boldsymbol{U}} \cdot \nabla \tilde{W} = -\frac{\partial \tilde{P}}{\partial \tilde{z}} + \frac{1}{Re_0} \tilde{\nabla}^2 \tilde{W} + \frac{1}{Fr} \tilde{\vartheta}, \tag{2.22}$$

$$\frac{\partial \tilde{\vartheta}}{\partial \tilde{t}} + \tilde{U} \cdot \nabla \tilde{\vartheta} = -\frac{1}{Fr} \tilde{W} K^2 + \frac{1}{Re_0 Pr} \tilde{\nabla}^2 \tilde{\vartheta}, \tag{2.23}$$

leaving only three dimensionless parameter groups in the equations: the Froude number $Fr = U_\alpha / N L_\alpha$, initial Reynolds number $Re_0 = U_\alpha L_\alpha / \nu$ and Prandtl number $Pr = \nu/\kappa$. Similarly, the source now has the form

$$\tilde{\Pi}_U = -\frac{1}{Re_0} \frac{\partial^2 \tilde{U}_b}{\partial \tilde{z}^2}, \quad \tilde{U}_b(\tilde{z}) = \exp(-\tilde{z}^2) \exp\left(\left(\frac{L_z \alpha}{L_z \alpha - \tilde{z}} \right)^2 \right) \exp\left(\left(\frac{L_z \alpha}{L_z \alpha + \tilde{z}} \right)^2 \right) \mathrm{e}^2. \tag{2.24}$$

The governing equations (2.1), (2.2), (2.16) and (2.17) are solved using numerical methods described in § 2.2. The parameters for this problem are κ, ν, $U_b(0)$, N, and α; their values used in our simulations are listed in table 1. Case 1 is regarded as the reference case. The viscous and thermal diffusivities are set to 1×10^{-4} and 1.4×10^{-4}, respectively, for cases 1–5 and 6×10^{-5} and 8.6×10^{-5} for case 6, resulting in a Prandtl number ν/κ of 0.7 in all cases as for air. Case 2 has higher and case 3 has lower stratification compared to case 1. The dependence on stratification can be studied through the first three cases. Cases 4, 5 and 6 have higher forcing, as evident from their respective Reynolds numbers. Cases 4 and 5 are simulated with a resolution of $256^2 \times 512$ while cases 1–3 have a resolution of $128^2 \times 512$. The largest Reynolds number simulation in case 6 has the highest resolution of $512^2 \times 1024$.

The vertical gradient of $U_b(z)$ is large in the middle region (except at $z = 0$) and correspondingly $Ri_g = (NK(z))^2/(\mathrm{d}U_b/\mathrm{d}z)^2$ is small there. The base jet profile is linearly unstable for $Ri_g < 0.25$. The shear is sufficiently large to overcome the stability due to stable stratification and the flow develops instabilities and turbulence. Based on the centreline velocity of the jet at the basic state $U_b(0)$ and α^{-1}, the initial Reynolds number is given in table 1. Cases 1, 2 and 3 have the same Reynolds number but different background stratification. Increasing the forcing parameter has the effect of increasing the Reynolds number (cases 4, 5 and 6). For the quasi-equilibrium turbulent state we define turbulent length and velocity scales as follows. The length scale, $L_d = q^3/\epsilon$ is based on the turbulent kinetic energy (TKE) dissipation ϵ and q (Batchelor 1953):

$$\epsilon = \nu \langle s_{ij} s_{ij} \rangle, \qquad q^2 = \langle u'^2 + v'^2 + w'^2 \rangle, \tag{2.25}$$

Case	1	2	3	4	5	6
Fr_d	1.26	0.41	5.21	1.98	2.54	1.11
Re_d	826	534	798	1392	2392	4016

TABLE 2. Values of parameter groups at quasi-equilibrium at the vertical level $\alpha z = 1.0$; $Fr_d = q/(N_{eq} L_d)$, $Re_d = q L_d/\nu$ are based on the length scale L_d; N_{eq} is defined in (3.1).

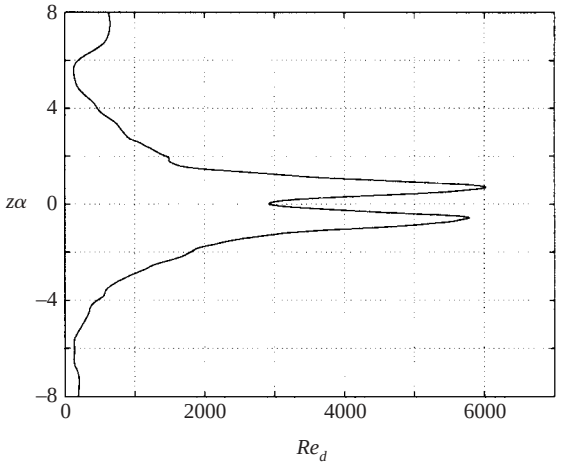

FIGURE 4. The Reynolds number based on the length scale L_d and q for $512^2 \times 1024$ resolution, case 6, $Re_d = q L_d/\nu$.

where $s_{ij} = \frac{1}{2}(\partial u_i/\partial x_j + \partial u_j/\partial x_i)$ is the rate-of-strain tensor (Pope 2000) and u_i and x_i ($i = 1, 2, 3$) correspond to our u, v, w and x, y, z notation respectively. The values of the turbulent Reynolds number Re_d and Froude number Fr_d with this set of scales are given in table 2 for the vertical level $\alpha z = 1.0$. The scales and the Reynolds number Re_d vary with vertical level, being highest near the edges of the jet, and decay rapidly away from the edges; see figure 4 for case 6 with $512 \times 512 \times 1024$ resolution.

2.2. *Numerical methods*

In the present study we use a spectral domain decomposition method, which is particularly suitable for simulation of flows with non-uniform background stratification and shear. The flow is assumed to be homogeneous only in the horizontal directions where periodic boundary conditions are used. For each horizontal wavenumber, the vertical domain is then broken down into several subdomains (figure 5). Each subdomain is separately mapped to a domain $\{-1 \leqslant z' \leqslant 1\}$. For non-overlapping subdomains, there are basically two solution methods: collocation and variational methods. In the collocation method, the variable (e.g. λ) within each subdomain j is interpolated as

$$\lambda^j(z') = \sum_{i=0}^{n} c_i^j \phi_i(z'), \qquad -1 \leqslant z' \leqslant 1, \tag{2.26}$$

where n is the order of interpolation, and the functions $\phi_i(z')$ are the Lagrange interpolants. The local coordinate z' is chosen to be the Gauss–Lobatto–Legendre point.

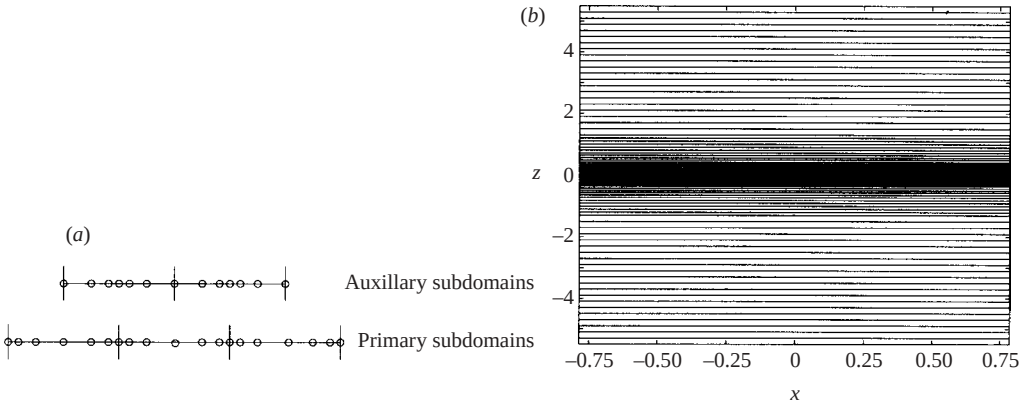

FIGURE 5. (*a*) Distribution of collocation points in primary and auxillary subdomains. The vertical lines separate the subdomains. (*b*) Distribution of primary subdomain boundaries in the vertical direction.

The differentiation of variables is carried out by differentiating the interpolants. An efficient routine for the differentiation exists; e.g. Fornberg (1996). The domain decomposition method, however, requires patching of subdomain boundaries when forming the global differentiation matrix. In inverting the second-order differentiation matrix (e.g. in calculating the pressure Poisson equation), continuity of the first-order derivative is required as the subdomain boundary condition. This is usually done by replacing $n-1$ rows (corresponding to $n-1$ subdomain boundaries) of the global matrix by the first-order derivative equations. This method, however, may lead to numerical disturbances at the subdomain boundaries, particularly if the resolution of the problem is marginal. To overcome this problem, an auxillary set of subdomains is defined, with each subdomain in the auxillary set straddling the subdomains in the primary set. The arrangement is shown schematically in figure 5. Another global differentiation matrix is then formed, and differentiation or integration are carried out by multiplication or inversion of a combination of these two matrices. When this method is used in the advection–diffusion equation, exponential convergence of accuracy is observed for linearly increasing order of interpolation. The method has been tested using the turbulent channel flow problem, and excellent performance has been found. Further details on the numerical method are given in Tse *et al.* (2001).

The time discretization follows the usual pressure projection method, which separates the time derivatives into three substeps. The nonlinear terms and buoyancy terms are advanced in the first substep; pressure Poisson equations are then solved directly and the pressure terms are advanced in the second substep while the dissipation terms are handled in the third substep. A second-order Adams–Bashforth scheme is used for the nonlinear terms. The calculation of derivatives involved in the nonlinear terms is carried out in physical space using a collocation method. The third substep requires calculating the viscous terms implicitly. A total of eight forward fast-Fourier transforms (FFT) and four backward FFT are required. The program is parallelized by the transposition method using the Message Passing Interface (MPI). In the vertical direction, absorption layers are added to the top and bottom boundaries to remove the reflection of waves. The computational box (shown in figure 5*b*) has a length of $\pi/2$ in both horizontal directions and extends from -5.0 to $+5.0$ in the vertical direction. Grid resolutions used in the simulations are either $128 \times 128 \times 512$,

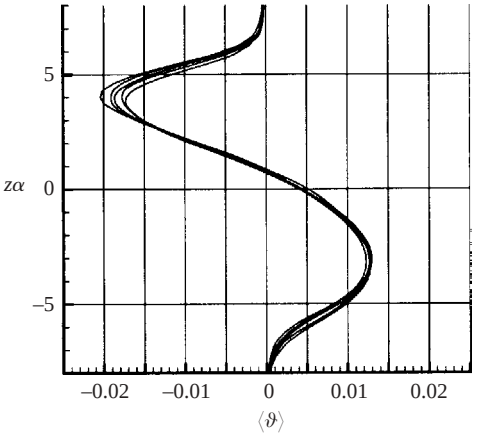

FIGURE 6. Evolution of the mean temperature, $\langle\vartheta\rangle$, at quasi-equilibrium, case 1.

$256 \times 256 \times 512$ or $512 \times 512 \times 1024$ (table 1). There are either 127 (for cases 1–5) or 255 (for case 6) subdomains in the vertical direction. The interpolation for the central three subdomains is fifth-order, and fourth-order elsewhere. The total number of grid points in the vertical is then equal to a power of two, avoiding the situation where one processor needs to carry an extra plane for computation. The width of the subdomains between -0.062 to 0.062 is 0.004, and the width gradually increases to 0.2 at the outer regions. The jet stream is located at the centre of the computational domain. This region requires more resolution due to higher shear (figure 5). The computations are performed on massively parallel supercomputers at Los Alamos National Laboratory and the DoD ARL MSRC.

2.3. *Quasi-equilibrium state*

Long-time integration of the governing equations (2.1)–(2.5) is affected by the presence of adiabatic invariants for the long-time dynamics. In particular, it has been shown in Babin, Mahalov & Nicolaenko (1998) that in the asymptotic state (after several periods of oscillations associated with wave motions; Mahalov, Nicolaenko & Zhou 1998) the horizontally averaged temperature $\langle\vartheta\rangle$ is a near-adiabatic invariant with only a small drift in time; this drift is confirmed by our DNS in figure 6. A state of absolute equilibrium is one where the mean temperature $\langle\vartheta\rangle$ as well as other (horizontally) averaged quantities are no longer changing with time. We recall the mean (horizontally averaged) temperature equation

$$\frac{\partial\langle\vartheta\rangle}{\partial t} + \frac{\partial\langle w'\vartheta'\rangle}{\partial z} = \kappa\frac{\partial^2\langle\vartheta\rangle}{\partial z^2}, \tag{2.27}$$

and define quasi-equilibrium to be a state where $\langle\vartheta\rangle$ satisfies (2.27) with a small but finite time derivative (slow steady drift as in figure 6) and where all other mean values are quasi-stationary and the integrated statistics of variances show little fluctuation ($< 5\%$). This is illustrated in figure 7 for a typical case where the vertically integrated values of velocity variances, $\int\langle u'^2\rangle\,\mathrm{d}z$ (I), $\int\langle v'^2\rangle\,\mathrm{d}z$ (II) and $\int\langle w'^2\rangle\,\mathrm{d}z$ (III), temperature variance $\int\langle\vartheta'^2\rangle\,\mathrm{d}z$ (IV) and the rate of change of horizontal velocity variance, $\int|\partial\langle u'^2\rangle/\partial t|\,\mathrm{d}z$ (V), are plotted against the large-eddy turnover time ($S_b^{-1} = (\max|\partial U_b/\partial z|)^{-1} \approx 0.018$). Our range for $S_b t$ is longer than those reported in typical homogeneous shear flow simulations since we are using the maximum value of shear at the basic state. All the curves initially overshoot and then settle down to a

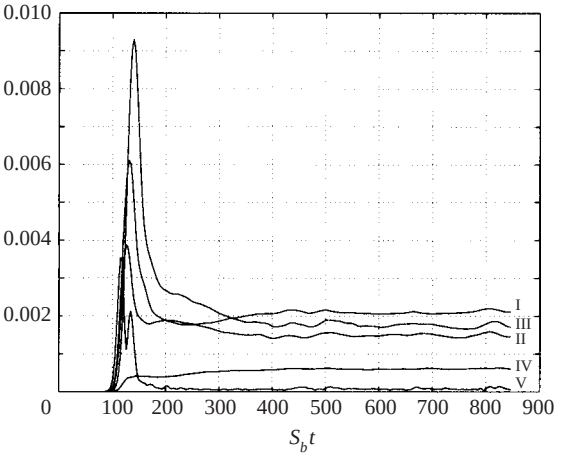

FIGURE 7. The time evolution of vertically integrated values of $\langle u'^2 \rangle$ (I), $\langle v'^2 \rangle$ (II), $\langle w'^2 \rangle$ (III), $\langle \vartheta'^2 \rangle$ (IV) and $|\partial \langle u'^2 \rangle / \partial t|$ (V); $\langle \cdot \rangle$ denotes horizontal averaging. Horizontal axis is given in non-dimensional time $S_b t$.

relatively constant value. The first stage of evolution corresponds to the onset of initial shear instabilities. Secondary instabilities then have an effect, and with transition to fully developed three-dimensional turbulence the variances drop and begin to saturate, with TKE production balancing the energy sinks. This is evident from the spectra in the quasi-equilibrium state presented in Tse *et al.* (2001), which span several decades. After the velocity variances become quasi-stationary, the horizontally averaged mean temperature is still evolving, albeit slowly, as shown in figure 6 for case 1. Physically, quasi-equilibrium states can be obtained if the synoptic-scale driving force has a much longer time scale (e.g. see figure 3 of Cullen 2002).

3. The mean profiles, variances and covariances

In this section, based on our long-time DNS, we present vertical profiles at quasi-equilibrium for the mean temperature, three velocity components and the corresponding variances and covariances. The mean (horizontal-averaged) velocity in the streamwise direction $\overline{U} = U_b + \langle u \rangle$ at quasi-equilibrium is shown in figure 8 for the cases from table 1. These plots are time-averaged over one large-eddy turnover time defined by $2\pi/(\alpha q)$. The vertical axis is non-dimensionalized by $1/\alpha$ and the velocity is non-dimensionalized by $\overline{U}(0)$. Hence the normalized values are all equal to unity at the centre. Cases 1, 2 and 3 are shown in figure 8(a) while cases 4, 5 and 6 are shown in figure 8(b). The profiles for cases 5 and 6 are essentially identical. The amount of stratification does not have much effect on the width of the mean flow, which is determined by the profile of the momentum source Π_U. There is a counterflow away from the central region. Note that the asymmetry generated by the doubling of the Brunt–Väisälä profile is more prominent in case 2 than in the other cases. The peak value of $\overline{U} = U_b + \langle u \rangle$ in this case is also larger than in other cases. In the decaying simulation by Galmiche *et al.* (2002), an increase of stratification has been observed to cause transfer of energy from turbulence to the mean.

The mean temperature profile $\langle \vartheta \rangle$, which is the mean of the perturbation of the basic profile, is a slowly evolving quantity that can serve as an indicator of a particular quasi-equilibrium state at that vertical level. It is plotted in figure 9, with values

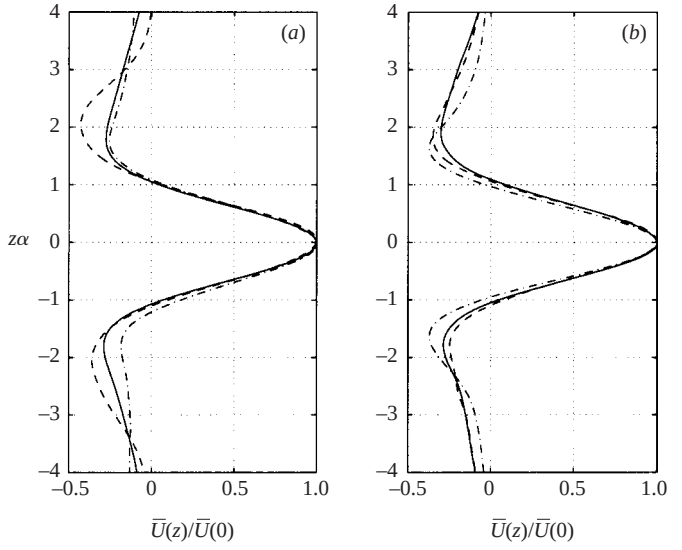

FIGURE 8. Normalized mean (horizontally averaged) velocity in the streamwise direction $\overline{U}(z)/\overline{U}(0)$ where $\overline{U} = U_b + \langle u \rangle$, for cases listed in table 1: (*a*) cases 1 (solid), 2 (dash) and 3 (dash-dot); (*b*) cases 4 (solid) , 5 (dash) and 6 (dash-dot).

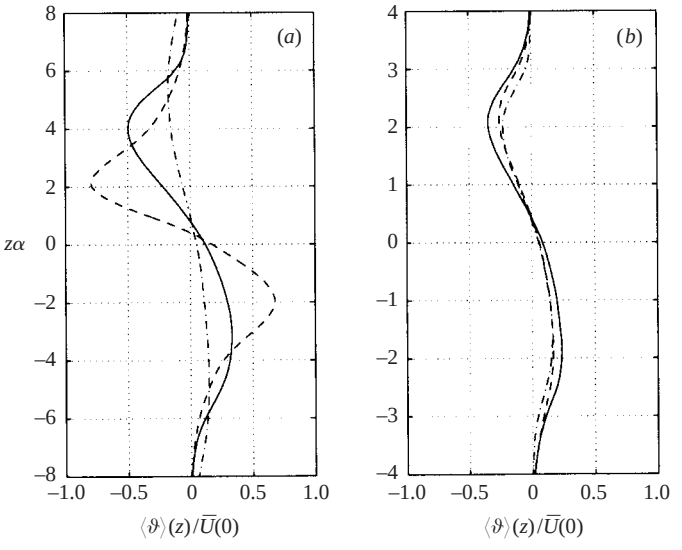

FIGURE 9. Normalized mean (horizontally averaged) temperature, $\langle \vartheta \rangle(z)/\overline{U}(0)$, in the quasi-equilibrium state for cases listed in table 1: (*a*) cases 1 (solid), 2 (dash) and 3 (dash-dot); (*b*) cases 4 (solid), 5 (dash) and 6 (dash-dot).

normalized by $\overline{U}(0)$ (ϑ has the unit of velocity). The values are negative in the upper domain and positive in the lower domain. As will be seen later in figure 20, the vertical heat flux is negative in the central region and it is very small elsewhere. As a result, the temperature decreases at the top and increases at the bottom due to buoyancy flux crossing the centre. In figure 9 the peaks for case 2 are the largest, followed by case 1 while case 3 has the smallest peaks. One prominent feature is that, as the

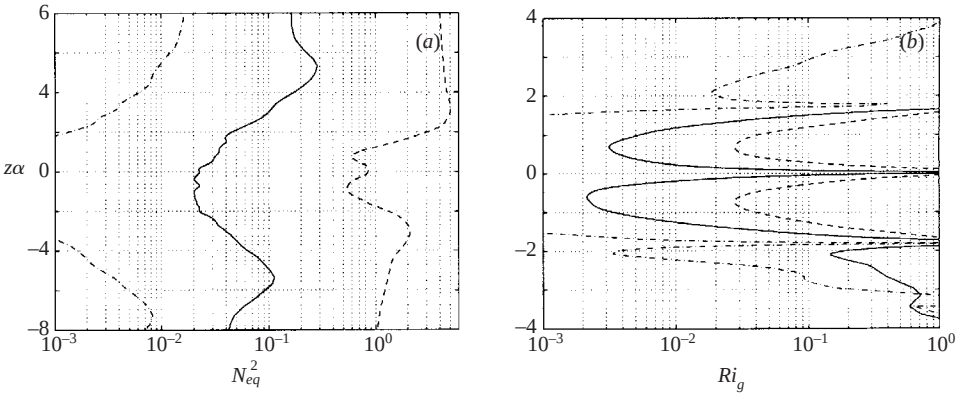

FIGURE 10. (*a*) The square of the Brunt–Väisälä frequency profile, N_{eq}^2, and (*b*) gradient Richardson number profiles at quasi-equilibrium from the numerical simulations for cases 1 (solid), 2 (dash) and 3 (dash-dot).

stratification decreases, the peaks move away from the core of the flow. Consider case 3 for example: $\langle\vartheta\rangle$ peaks at $z\alpha \approx 5.36$ and -4.96, at distances significantly away from the sides of the jet at $z\alpha \approx \pm 1$. There are no significant differences in the location of peaks for cases 4, 5 and 6.

Figure 10(*a*) shows profiles of the turbulent-mean-state squared Brunt–Väisälä (buoyancy) frequency. A dramatic decrease in the jet core, through turbulent mixing, is clearly noticed. A Brunt–Väisälä profile of this kind, with a localized minimum in the mixing region, is sometimes referred to as possessing a 'notch'. It is known to be a mean-state configuration favouring emission of gravity waves from tropospheric jet streams (Lott, Kelder & Teitelbaum 1992; Sutherland & Peltier 1995). We note that although the basic-state Brunt–Väisälä profile has only a smooth doubling at the jet levels, the time-varying mean state in our DNS evolves to a profile having such a notch configuration. Nastrom & Eaton (1997) found a localized decrease of the Brunt–Väisälä parameter at the tropopause level in several winter seasonal profiles, which adds credence to our simulation results (cf. their figure 5*b*). Vertical profiles of the gradient Richardson number $Ri_g = N_{eq}^2/(\partial\overline{U}/\partial z)^2$ at the quasi-equilibrium are shown in figure 10(*b*) for cases 1, 2 and 3, where

$$N_{eq}^2 = N\mathrm{d}\langle\vartheta\rangle/\mathrm{d}z + N^2K^2(z) \tag{3.1}$$

is the normalized Brunt–Väisälä frequency profile at quasi-equilibrium. The gradient Richardson number Ri_g profile at quasi-equilibrium is very similar to those obtained by Bedard *et al.* (1986) as shown in figure 3(*a*) and to the profiles for cases 4, 5 and 6 in figure 3(*b*). Comparing cases 1, 2 and 3, we can see that an increase of stratification causes the curves of Ri_g to move closer to the core. On the other hand, an increase or decrease in the forcing term also changes the vertical position of the Ri_g curves, which is clear when we compare cases 1 and 5.

Visualizations of the flow fields are shown in figures 11–14 for a better understanding of the flow structure. The velocity vectors, fluctuation temperature, spanwise vorticity and local gradient Richardson number on a typical vertical-plane cross-section (where the horizontal scale is taken to be αx) are plotted here for cases 1 and 2. As can be seen in figure 11(*a*), counterclockwise rollers appear on top and clockwise rollers appear on the bottom edge of the jet. This agrees with the contour levels of the spanwise vorticity in figure 12(*a*). Entraining fluid from above and below the jet

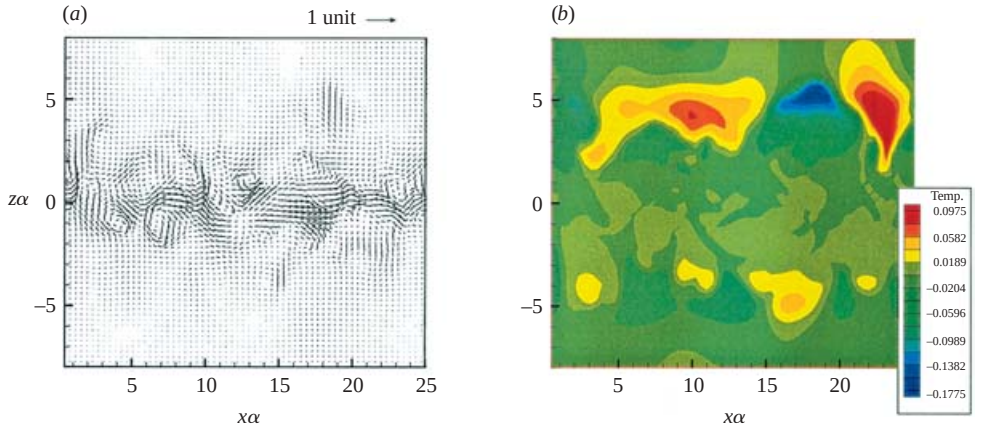

FIGURE 11. (*a*) Instantaneous velocity vectors and (*b*) temperature fluctuation on a vertical plane for case 1. Magnitude of velocity is given by arrow length.

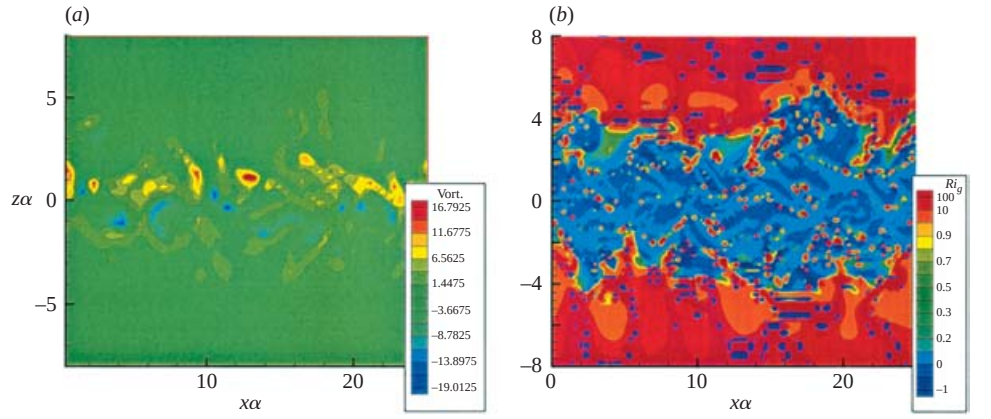

FIGURE 12. (*a*) Instantaneous spanwise vorticity and (*b*) local gradient Richardson number on a vertical plane for case 1.

generates fingers of hot and cold fluid, as evident from temperature contours shown in figure 11(*b*). The temperature fluctuation at the centre is comparatively small. Figure 12(*b*) shows the local gradient Richardson number at the same vertical-plane cross-section. High values are obtained away from the core while values close to the centre are small. Peaks of temperature variance (see also figure 18) are shifted relative to peaks of velocity variances shown in figures 15 and 16. These results are consistent with atmospheric observations of Nastrom *et al.* (1986).

The fields for case 2 are plotted in figures 13 and 14 (stronger background stratification compared to case 1). The vortices and the waviness are observed in the vector projections (figure 13*a*). The corresponding spanwise vorticity field shown in figure 14(*a*) has high-intensity zones concentrated around the centre. The most significant difference between cases 1 and 2 is the amplitude of temperature fluctuations, which is intensified in case 2. The maxima of temperature fluctuations in case 2 are closer to the core; that is $z\alpha \approx 2$ instead of $z\alpha \approx 5$ in case 1 (cf. figure 18*a*). The local gradient Richardson number shown in figure 14(*b*) is not significantly different from case 1.

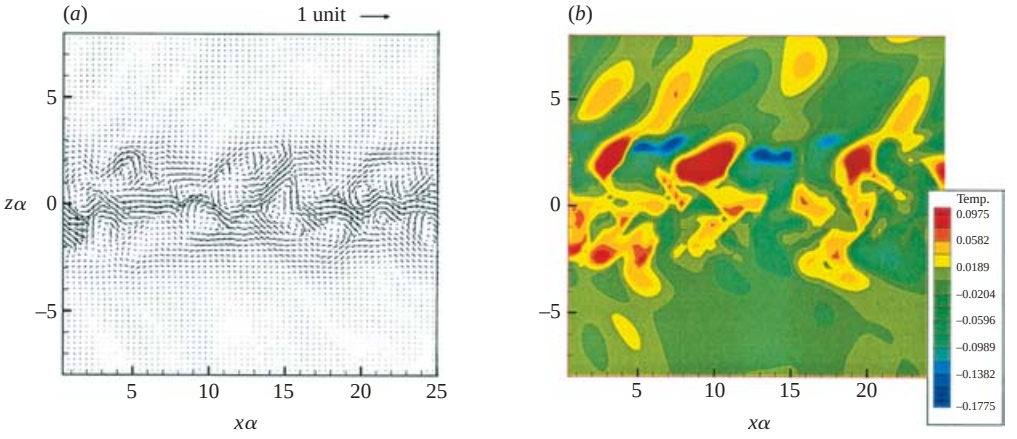

FIGURE 13. (*a*) Instantaneous velocity vectors and (*b*) fluctuating temperature component on a vertical plane for case 2.

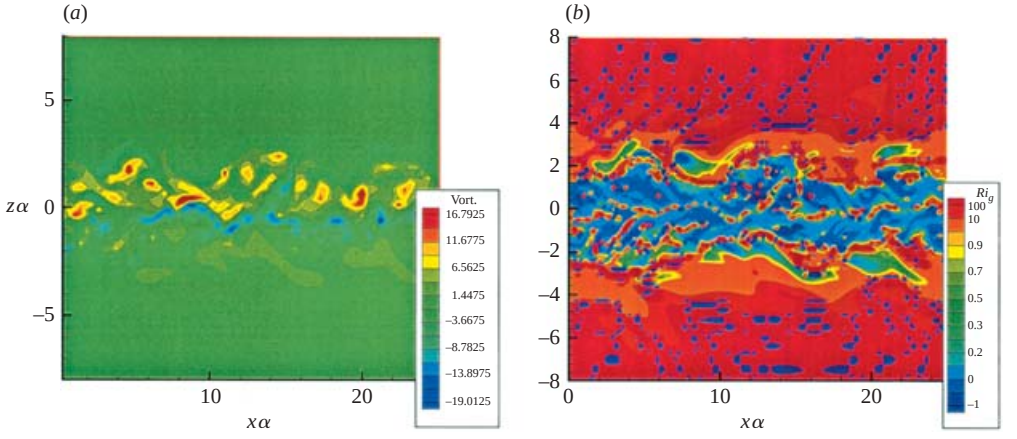

FIGURE 14. (*a*) Instantaneous spanwise vorticity and (*b*) local gradient Richardson number on a vertical plane for case 2.

The variances of the streamwise velocity, $\langle u'^2\rangle/\overline{U}(0)^2$ are shown in figure 15. Cases 1, 3, 4 and 5 have similar magnitudes while case 2 has the smallest normalized variance. In general, the variances show two peaks located roughly at the edges of the jet, at $z\alpha \approx \pm 0.70$ where $\partial U_b/\partial z$ is largest. This agrees with observations of Beland (1993) that the turbulence intensity is highest at the edges of the jet stream. The value of $\langle u'^2\rangle/\overline{U}(0)^2$ is the lowest in case 2, and decays more rapidly away from the core due to the higher stratification. In contrast, the values for cases 1 and 3 are similar, suggesting that stratification in these cases is too low to have any significant effect on velocity variances. This is also true for cases 4 and 5. The variances of the spanwise velocity $\langle v'^2\rangle/\overline{U}(0)^2$ are shown in figure 16. Their vertical profiles exhibit two peaks, but their magnitudes are generally much smaller than those of corresponding streamwise components. Vertical velocity variances $\langle w'^2\rangle/\overline{U}(0)^2$ are presented in figure 17. They show a single peak at the centre of the jet core. Again, case 2 is significantly smaller in value than cases 1 and 3, in view of the increased stratification. The magnitudes

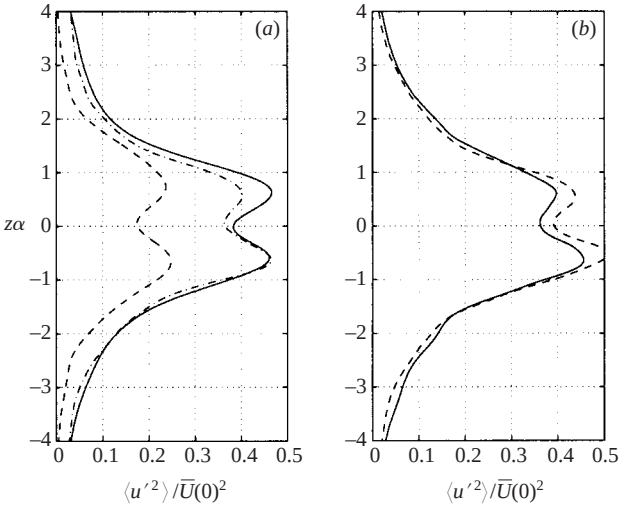

FIGURE 15. The normalized variances of the streamwise velocity, $\langle u'^2\rangle/\overline{U}(0)^2$ as a function of the normalized height: (*a*) cases 1 (solid), 2 (dash) and 3 (dash-dot); (*b*) cases 4 (solid) and 5 (dash).

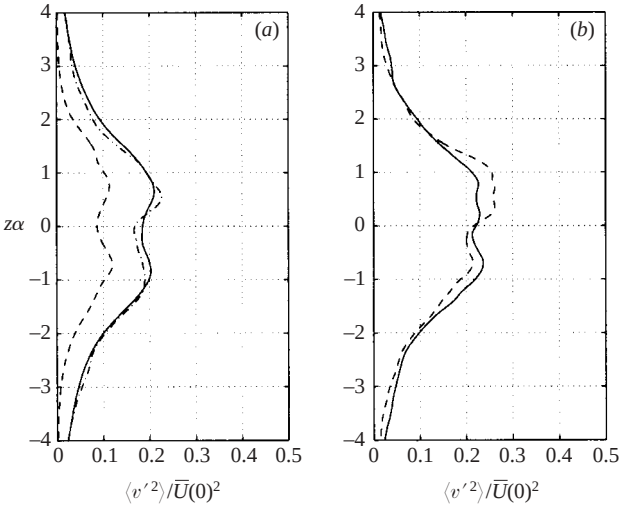

FIGURE 16. The normalized variances of the spanwise velocity, $\langle v'^2\rangle/\overline{U}(0)^2$: (*a*) cases 1 (solid), 2 (dash) and 3 (dash-dot); (*b*) cases 4 (solid) and 5 (dash).

for cases 4 and 5 are roughly the same as in cases 1 and 3. The mean velocity profiles and profiles of $\langle w'^2\rangle/\overline{U}(0)^2$ agree qualitatively with recent water tank experiments on stratified and unstratified jets by Webster & Liu (2001). For unstratified jets, they obtained self-similar profiles for $\langle w'^2\rangle/\overline{U}(0)^2$ whereas self-similarity was not evident in stratified jets. The profiles of $\langle w'^2\rangle/\overline{U}(0)^2$ also agree qualitatively with those measured by Nastrom & Eaton (2001) in the lower stratosphere from VHF radar observations.

The normalized temperature variances $\langle \vartheta'^2\rangle/\overline{U}(0)^2$ in figure 18 show a trend opposite to that of the vertical velocity in that the former peaks while the latter drops to small values. The asymmetry in all cases is very prominent, a result of the

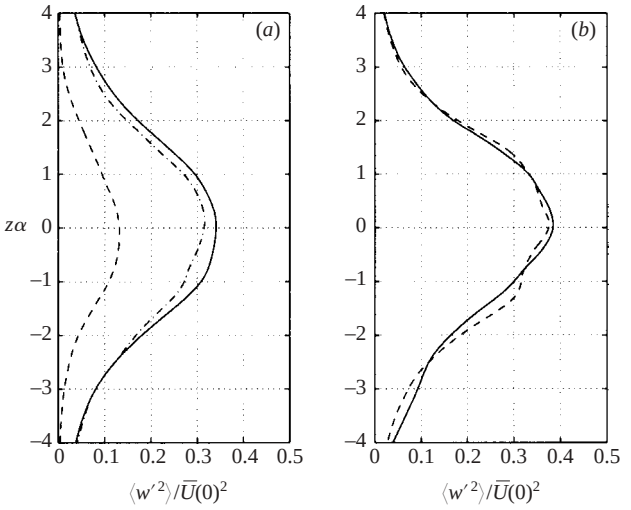

FIGURE 17. The normalized variances of the vertical velocity, $\langle w'^2\rangle/\overline{U}(0)^2$: (*a*) cases 1 (solid), 2 (dash) and 3 (dash-dot); (*b*) cases 4 (solid) and 5 (dash).

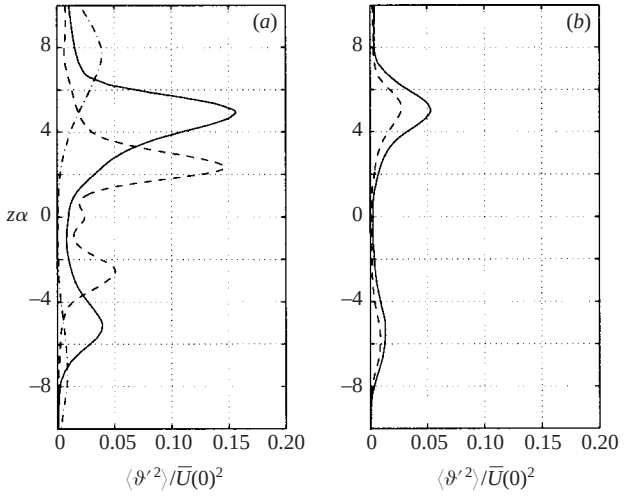

FIGURE 18. The normalized variances of the temperature, $\langle \vartheta'^2\rangle/\overline{U}(0)^2$: (*a*) cases 1 (solid), 2 (dash) and 3 (dash-dot); (*b*) cases 4 (solid) and 5 (dash).

jump in the Brunt–Väisälä frequency profile at the centre. As stratification decreases, the temperature fluctuations penetrate deeper into the surrounding fluid, spreading the peak of temperature variance further. In case 2, the upper peak of $\langle \vartheta'^2\rangle/\overline{U}(0)^2$ is located at $z\alpha \approx 2.4$, in case 1 at $z\alpha \approx 5$ and in case 3 at $z\alpha \approx 8$, which are somewhat further away from the core than the extrema of $\langle \vartheta \rangle$. The vertical levels of peaks for $\langle \vartheta'^2\rangle/\overline{U}(0)^2$ tend to vary inversely with the strength of stratification. For cases 4 and 5, the temperature variance peaks roughly at the same vertical levels as in case 1. However, the magnitude of the peaks decreases as the Reynolds number increases.

The normalized horizontal heat fluxes, $\langle u'\vartheta'\rangle/\overline{U}(0)^2$, are plotted in figure 19. They are negative immediately above the centre and positive below the centre. This is most prominent in case 2. This is in agreement with the previously discussed figures 11

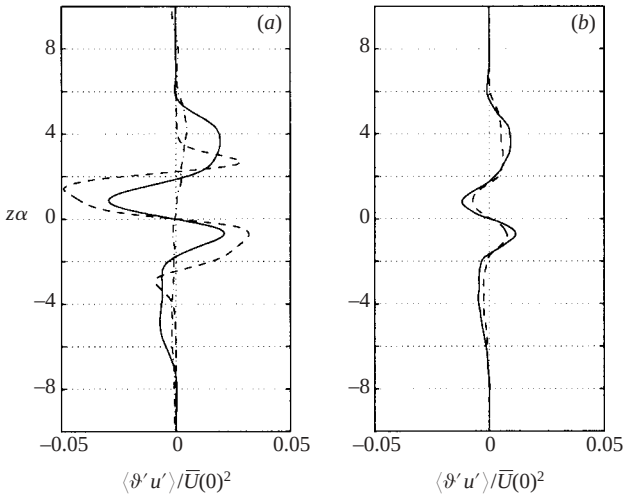

FIGURE 19. The normalized profile of the horizontal heat flux, $\langle \vartheta' u' \rangle / \overline{U}(0)^2$: (*a*) cases 1 (solid), 2 (dash) and 3 (dash-dot); (*b*) cases 4 (solid) and 5 (dash).

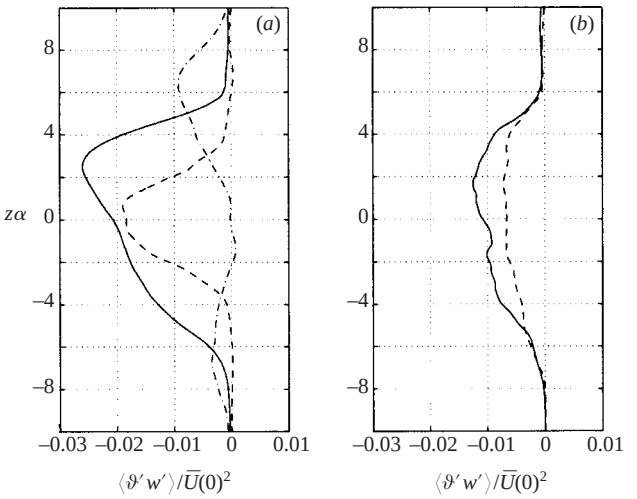

FIGURE 20. The normalized profile of the vertical heat flux, $\langle \vartheta' w' \rangle / \overline{U}(0)^2$: (*a*) cases 1 (solid), 2 (dash) and 3 (dash-dot); (*b*) cases 4 (solid) and 5 (dash).

and 13 where fingers of hot fluid are entrained into the core from above and fingers of cold fluid from below. Further away from the jet, $\langle \vartheta' u' \rangle$ changes its sign again. This is caused by the counterflow which carries cooler fluid to the top and hotter fluid to the bottom, resulting in positive and negative secondary peaks above and below, respectively. The normalized streamwise heat fluxes show strong dependence on the vertical level. The vertical heat fluxes $\langle w' \vartheta' \rangle / \overline{U}(0)^2$ are plotted in figure 20. For cases 1, 2 and 3, they are all negative, confirming that the heat is moving from the hotter (lighter) upper domain to the cooler (heavier) lower domain (down-gradient). Counter-gradient heat flux ($\langle w' \vartheta' \rangle$ positive) has been observed in others studies only when the gradient Richardson number is relatively large ($Ri_g \approx 0.5 - 1.0$, Gerz *et al.* 1989). For case 3, the heat flux is almost zero at the centre, corresponding to the near-neutral stratification. The peaks of $\langle \vartheta \rangle$, figure 9 are situated further away in the

	Case 1		Case 2		Case 3		Case 4		Case 5	
$\langle u'^2\rangle/q^2$	0.4214	0.4442	0.4448	0.5266	0.4293	0.4183	0.3738	0.3774	0.3971	0.3725
$\langle v'^2\rangle/q^2$	0.2037	0.2206	0.2207	0.2470	0.1989	0.2428	0.2300	0.2431	0.2221	0.2729
$\langle w'^2\rangle/q^2$	0.3750	0.3352	0.3344	0.2264	0.3719	0.3388	0.3962	0.3796	0.3808	0.3546
$-\langle u'\vartheta'\rangle/u'_{rms}\vartheta'_{rms}$	0.0162	0.3704	0.0169	0.5908	0.0275	−0.0260	0.0028	0.3251	−0.026	0.3114
$-\langle w'\vartheta'\rangle/w'_{rms}\vartheta'_{rms}$	0.3553	0.3480	0.3261	0.3740	0.0108	0.0136	0.3351	0.3611	0.3480	0.3120
$\langle u'w'\rangle/u'_{rms}w'_{rms}$	0.0041	0.5455	−0.0168	0.5322	0.0086	0.5248	0.0044	0.5207	−0.0173	0.5037

TABLE 3. Normalized values of variances and covariances at $z\alpha = 0$ and $z\alpha = 1$.

vertical than the peaks of $\langle w'\vartheta'\rangle$. In figure 20, the profiles of $\langle w'\vartheta'\rangle/\overline{U}(0)^2$ for cases 1, 2 and 3 are significantly different. If the profiles are not normalized (not shown here), case 2 has the largest peak at the core of the flow. When stratification decreases, the amount of heat flux at the core of the flow decreases, until it drops nearly to zero for case 3. At the same time, the heat flux at the edges increases and generates two peaks at $z\alpha \approx 7$ and -6.5 in case 3. The doubling of the Brunt–Väisälä profile results in the asymmetry of the heat flux profiles.

The anisotropy of the velocity components can be observed from table 3, which shows the normalized values of variances and covariances for several cases at the vertical levels $z\alpha = 0$ (centre) and $z\alpha = 1$ (edge region). The total fluctuating kinetic energy $q^2/2$ in table 3 is defined in (2.25). The *rms* subscript denotes the square root of variance (e.g. $u'_{rms} = \sqrt{\langle u'^2\rangle}$, etc). Generally, $\langle u'^2\rangle/q^2$ and $\langle w'^2\rangle/q^2$ together contribute roughly 80% of the kinetic energy with $\langle v'^2\rangle/q^2$ contributing the rest. The contribution from the vertical direction is smaller for higher stratification (case 2). Furthermore, the anisotropy decreases for cases 4 and 5 where the Reynolds number is higher. Anisotropy in stably stratified mixing layers has been studied by Smyth & Moum (2000). They found that the vorticity anisotropy tensor becomes isotropic as the Reynolds number increases. Velocity has a similar trend, but it is possible that in real atmospheric situations some degree of anisotropy will be retained (Vinnichenko 1980; Gargett, Osborne & Nasmyth 1984). Recent observations of turbulence around a winter jet stream using the 'Egrett' meteorological research aircraft show that anisotropy indeed persists at the smallest scale observed (~ 1 m) (Cote *et al.* 2003).

4. Variability of length scales and gradient Richardson number

The behaviour of stably stratified turbulent flows can be characterized in terms of length scales by which the relative magnitude of buoyancy, shear, inertial and viscous influences are signified. Some commonly used length scales are the shear length scale L_s, Ellison scale L_e, buoyancy scale L_b and Ozmidov scale L_o, defined in table 4. Relationships between these length scales have been investigated extensively, for example, in the atmospheric boundary layer by Hunt *et al.* (1985), through atmospheric radar observations by Eaton & Nastrom (1998), in ocean shear layers by Moum (1996), in numerical simulations by Itsweire *et al.* (1993) and using laboratory experiments (Rohr *et al.* 1988; De Silva & Fernando 1992); see Fernando (2002) for a discussion. The ratios of these length scales usually yield some important non-dimensional parameters, for example, $Ri_g = L_s^2/L_b^2$.

Buoyancy forces tend to influence the motion scales that are larger than certain 'outer' scales (Ozmidov, buoyancy, Ellison and shear). Scales that are smaller than

	Streamwise	Spanwise	Vertical	Other
Kolmogorov scale, L_η^2	–	–	–	$\left(\nu^3/\epsilon\right)^{1/2}$
Shear scale, L_s^2	$\langle u'^2\rangle/(\mathrm{d}\overline{U}/\mathrm{d}z)^2$	–	$\langle w'^2\rangle/(\mathrm{d}\overline{U}/\mathrm{d}z)^2$	$q^2/(\mathrm{d}\overline{U}/\mathrm{d}z)^2$
Ellison scale, L_e^2	–	–	–	$\langle\theta'^2\rangle/\left(\partial\overline{\vartheta}/\partial z\right)^2$
Buoyancy scale, L_b^2	–	–	$\langle w'^2\rangle/N_{eq}^2$	q^2/N_{eq}^2
Ozmidov scale, L_o^2	–	–	–	ϵ/N_{eq}^3

TABLE 4. Definition of length scales.

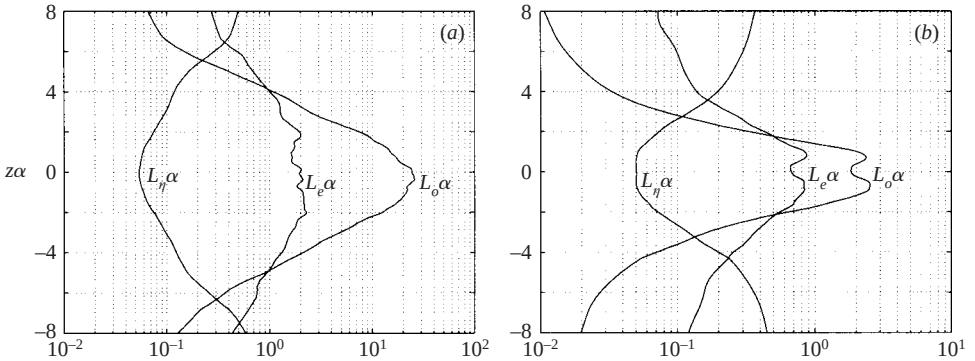

FIGURE 21. The normalized length scales $L_\eta\alpha$, $L_e\alpha$ and $L_o\alpha$ for (*a*) case 1 and (*b*) case 2 (logarithmic scale).

the outer scale but larger than the Kolmogorov scale show active three-dimensional turbulence. For larger $Ri_g > 1$ cases, the Ozmidov scale L_o is regarded as the outer scale above which the turbulence is significantly affected by buoyancy (cf. Phillips 1972, 1991). The Ellison scale L_e indicates the typical vertical distance travelled by fluid particles before either returning towards their equilibrium level or mixing (Rohr *et al.* 1988). The ratio $L_s/L_b = Ri_g^{1/2}$ accounts for the relative scales of influence of shear and buoyancy. If $L_s/L_b > 1$, then the buoyancy influence occurs at a scale smaller than the shear scale, and if active turbulence exists, then $\epsilon \sim (w'^2)^{3/2}/L_b$ and hence $L_b \sim (w'^2)^{1/2}/N \sim (\epsilon L_b)^{1/3}/N \sim L_o$ indicating that the Ozmidov scale L_o represents the scale beyond which the turbulent eddies are influenced by stratification (Fernando & Hunt 1996). In general, however, L_o should be contrasted with the buoyancy scale L_b at which the fluid parcel displacements (either due to turbulence or waves) are constrained by buoyancy forces. The Kolmogorov scale L_η characterizes the smallest scale of active turbulence and thus $L_o \sim L_\eta$ implies the complete suppression of active turbulence by stratification, leaving 'fossil' turbulence that mainly consists of nonlinear waves. Given that both L_b and L_e respond to the presence of waves and turbulence alike, Hunt *et al.* (1985) have suggested that the ratio L_e/L_b, the so-called temperature fluctuation parameter, is insensitive to the presence of waves, with an estimated value of $L_e/L_b = 1.0 \pm 0.5$. As is evident from the above discussion, for the weakly stable case of $Ri_g < 1$ with intense turbulence, the Ozmidov scale has a limited significance.

In figure 21(*a*, *b*) three normalized (by $1/\alpha$) length scales L_o, L_e and L_η are compared for cases 1 and 2, respectively. Note the difference in vertical variability of different length scales. While L_e and L_o peak roughly at the jet core, L_η reaches

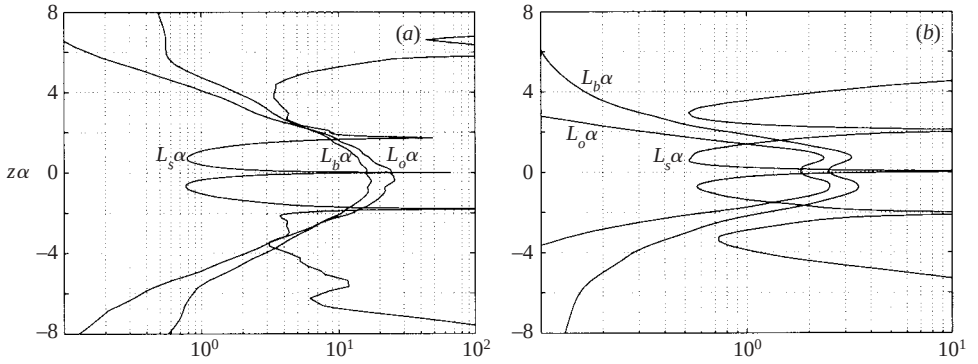

FIGURE 22. The normalized length scales $L_s\alpha$, $L_b\alpha$ and $L_o\alpha$ for (*a*) case 1 and (*b*) case 2 (logarithmic scale).

a minimum there; this scale separation is indicative of active turbulence with strong mixing, concurrent with low Ri_g values in the core (figure 10*b*). The ratio of L_o/L_η decreases markedly along the jet edges, pointing to the inhibition of turbulent mixing and fossilization of turbulence at $z\alpha \approx \pm 6$. Beyond these vertical levels, turbulent fluctuations (figures 15–18) and the vertical heat flux (figure 20) are drastically reduced. The scales L_e and L_o in the upper domain drop faster than in the lower domain because of higher stratification. Figure 21(*b*) is a plot of length scales for case 2, which is generally similar to case 1. The Kolmogorov scale remains unchanged, but two peaks of L_o can be seen in the jet shear layers. However, the positions where $L_\eta \approx L_o$ and $L_\eta \approx L_e$ now occur at a much lower vertical levels $z\alpha \approx \pm 3$, a signature of decreased spatial influence of the jet due to increased stratification. These observations are consistent with the fields shown in figures 11–14. The decades of separation between L_η and the outer scales in the zone of active turbulence do guarantee the effective resolution of all outer scales. For case 2, figure 21(*b*), L_e becomes greater than L_o for $z\alpha > 2$ (the ratio L_e/L_o crosses unity at $z\alpha \approx 2$); from figure 10(*b*) these are also the vertical levels where $Ri_g > 0.25$, with pronounced temperature fluctuations and very patchy turbulence in that region. This is in general agreement with figure 10 of Schumann & Gerz (1995) who have plotted ratios of L_e/L_o vs. Richardson number and observed $L_e/L_o < 1$ for Ri_g small, and $L_e/L_o \approx 1$ at $Ri_g \approx 0.25$ (in the context of uniform linear vertical shear and stratification).

Figure 22(*a*, *b*) shows the variations of L_o, L_b and L_s for cases 1 and 2, respectively. In figure 22(*a*), within the jet core $|z\alpha| < 2$ (except at the centre) $L_s \ll L_b$, indicating a low $Ri_g (\ll 1)$, conditions prone for instabilities and turbulence. In the core $L_o \gg L_s$ and $L_o \approx L_b$ indicating that turbulence in this region is active and intense. Note that $L_s < L_b$ implies that the vertical fluid parcel displacements are sufficiently large to be deformed by the mean shear, promoting the interaction between Reynolds stresses and mean shear to yield sustained turbulence in the core ($|z\alpha| < 2$), which is clear from figures 15–19. In the highly stratified case 2 (figure 22*b*), L_o becomes smaller than L_b in the core, but both of them remain larger than L_s.

Since Ri_g is small (< 0.25) in the jet core (except at the centre $z\alpha = 0$), the turbulence therein is intense and the temperature is well mixed, leading to low temperature fluctuation levels (figures 3*b*, 11*b*, 18). In the higher-Ri_g region where buoyancy-dominated turbulence prevails, temperature fluctuations become maximum, thus providing conditions for higher optical turbulence. This is a region of interest where the length scale ratio $L_o/L_b < 1$ and where significant wave activity is expected

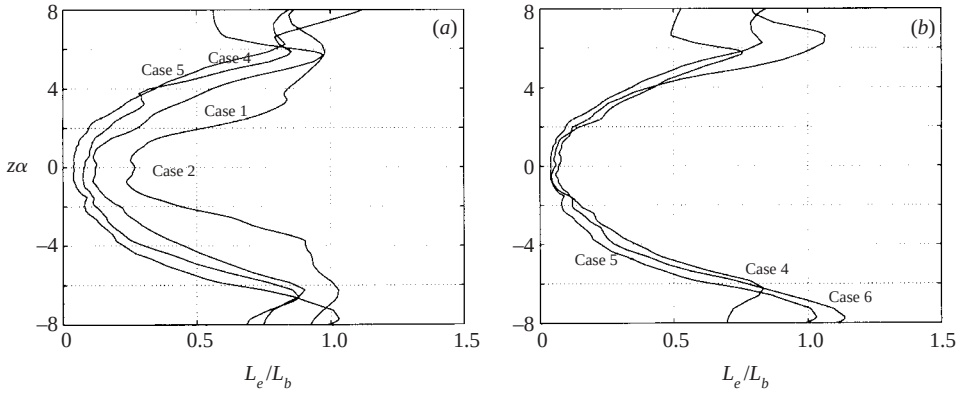

FIGURE 23. Ratio L_e/L_b for (*a*) cases 1, 2, 4 and 5 and (*b*) cases 4, 5 and 6.

(figure 24*a*, below). Therein the fluctuations are large, but there is not enough turbulent dissipation, pointing to the wave activity. Detailed energy budgets (see § 5, figures 25 and 26) show that in this region the shear production is vanishing and the energy is received via transfer from the jet core region. However, the energy deposited in this region by the pressure–velocity term is much smaller (and sometime negative) than that gained by the nonlinear terms, and hence the wave activity appears to be dominated by nonlinear waves. These results are in agreement with the laboratory experiments of Sutherland & Linden (1998) who found generation of large-amplitude internal waves in strongly stratified regions abutting weakly stratified turbulent regions. Given that the wave energy does not propagate beyond $|z\alpha| \approx 6$, these nonlinear waves are expected to break and cause intermittent turbulent patches in the region $2 < |z\alpha| < 6$, which is consistent with low local Ri_g regions of figures 12(*b*) and 14(*b*). Such breaking events can sustain some heat flux (as shown in figures 19 and 20) in this layer while maintaining significant temperature fluctuations.

At the edges of the jet (case 1, figure 22*a*), in a thin layer around $|z\alpha| \approx 1.8$, we have $L_s > L_o, L_b$ indicating that turbulence production by shear and Reynolds stress interaction is impeded. Ri_g in this region is large (figure 3*b*) and hence active turbulence is possible when Ri_g locally and intermittently drops below a critical value. Figures 11–14 show that indeed the turbulence is intermittent at the jet edges. At larger distances from the jet centre, $2.2 < |z\alpha| < 4$, $L_b \sim L_s$, indicating marginal conditions for the maintenance of stratified turbulence; figure 12 shows that turbulence in this region is very patchy. Also, pronounced temperature fluctuations in this region (with $L_e > L_o$ for case 2) points to possible wave activity. For $|z\alpha| > 4$, the scales L_o and L_b are markedly smaller than L_s, confirming the lack of sustained turbulence. This is generally consistent with figures 11–14 and velocity variances shown in figures 15–17.

Other length scale ratios are also of interest. As stated above Hunt *et al.* (1985) predicted L_e/L_b of unity in stable atmospheric boundary layers dominated by waves and turbulence, and found a ratio of about 0.8 in their field measurements. The ratios of L_e/L_b in our DNS for cases 1, 2, 4 and 5 are plotted in figure 23(*a*). The ratio is smallest around the centre of the jet and increase at the edges. It drops to 0.1 at the centre for case 1. In the core, L_e/L_b for case 2 (with strong stratification) is higher (≈ 0.25) than that of case 1 indicating that turbulence is more buoyancy influenced. At the centre, the ratios for cases 4 and 5 are even smaller than for case 1. For all cases, the ratios increase close to unity away from the core, indicating the

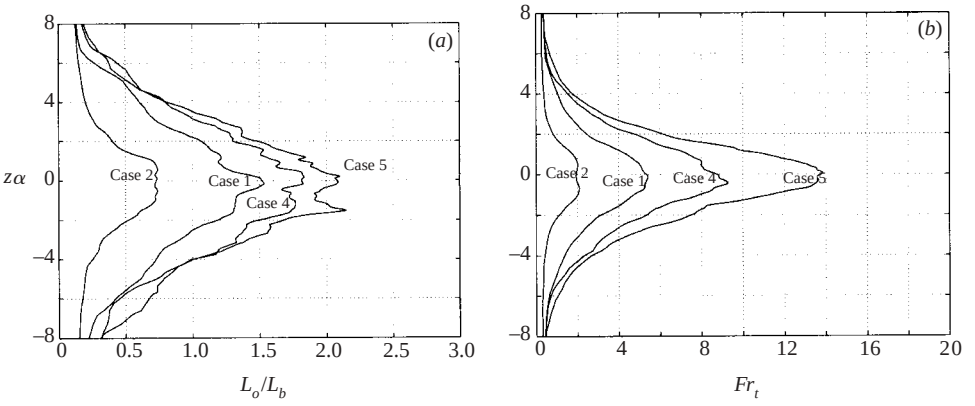

FIGURE 24. (*a*) Ratio L_o/L_b for cases 1, 2, 4 and 5. (*b*) The turbulent Froude number, $Fr_t = (L_o/L_e)^{2/3}$ for cases 1, 2, 4 and 5.

increasing importance of wave–turbulence activities at such vertical levels. In case 2, the ratio approaches a peak value of unity at around $z\alpha \approx \pm 4$, while for cases 1, 4 and 5, the peaks of L_e/L_b are observed at $z\alpha \approx \pm 6$. From figure 18, these peaks approximately correspond to the observed peaks of $\langle\theta'^2\rangle$ for both cases 1 and 2. Higher stratification pushes the vertical peak levels of the ratio closer to the core; such peaks are signatures of zones of stratified turbulence. It should be noted that the usual techniques of the phase spectra of vertical velocity and temperature, which show a phase angle of 90° for linear internal waves (Stewart 1969), and 'penetration condition' used by Sutherland & Peltier (1993, 1995) are not suitable for the nonlinear waves emanating from the highly three-dimensional flow configuration used here.

Figure 24(*a*) shows the ratio L_o/L_b, which is an indicator of the levels of turbulence and waves; when $L_o/L_b < 1$, the wave activity is considered dominant over turbulence and vice versa. Note how this ratio changes over the vertical spread of the jet. The value of $L_o/L_b \sim 1$ observed outside the jet core in the shear layer is roughly the same as that measured by Hebert *et al.* (1992) in a turbulent patch in the Pacific equatorial (jet-like) undercurrent (see also Moum 1996). The ratio $(L_o/L_e)^{2/3}$ is sometimes called the turbulent Froude number, Fr_t and is an alternative to the bulk Richardson number (Shih *et al.* 2000). Fr_t for cases 1, 2, 4 and 5 is plotted in figure 24(*b*). The curves are bell shaped, with cases 4 and 5 having the largest values, followed by case 1 and then case 2. The values at the core are all larger than unity, but Fr_t drops to less than unity in regions where the stratification is dominant. In laboratory grid-generated salt-stratified turbulence, Rohr *et al.* (1988) have measured the ratio L_e/L_o from which the corresponding turbulent Froude numbers Fr_t can be deduced. For $N = 0.961\,\mathrm{s}^{-1}$, they obtain values for L_e/L_o from 0.1 to 1.8 as the downstream position increases, which correspond to $(L_o/L_e)^{2/3}$ values of 4.6 to 0.68. The latter values are in the same range as those in figure 24(*b*).

5. Budgets

Budget terms were computed in the quasi-equilibrium state in order to characterize turbulent transport processes occurring at various vertical levels. Our budget equations presented in this section are based on the decomposition of velocity, temperature and pressure fields into the mean (horizontally averaged) and fluctuating components u', v', w', θ' and p', according to (2.6)–(2.10). The budget equations (5.1)–(5.4) are obtained

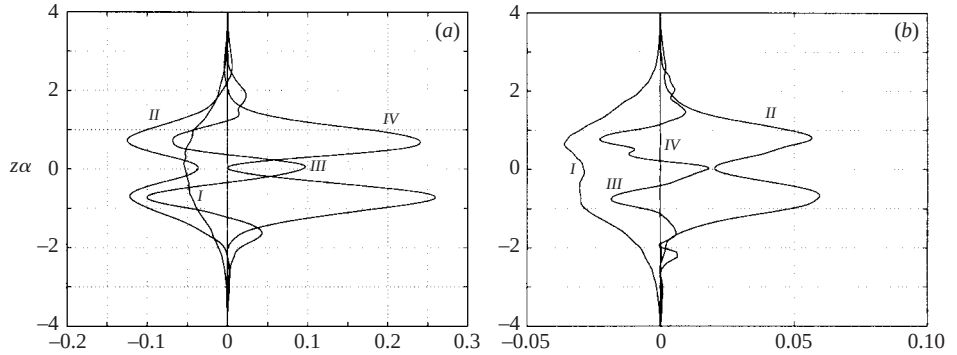

FIGURE 25. (*a*) The normalized horizontally averaged budgets in the equation for the streamwise velocity variance for case 2. (*b*) The normalized budgets in the equation for the spanwise velocity variance. Labels in the figures correspond to I – dissipation, II – pressure, III – transport and IV – shear production (term IV is nearly zero in *b*).

after substitution of the decomposition (2.6)–(2.10) into the governing equations and performing operations of horizontal averaging $\langle\ \rangle$; see Stull (1988). We report the budget terms of $\langle u'^2\rangle$, $\langle v'^2\rangle$, $\langle w'^2\rangle$ and $\langle \vartheta'^2\rangle$ for the highly stratified case 2.

The budget equation for $\langle u'^2\rangle$ is

$$\left.\begin{aligned} &\frac{\partial}{\partial t}\langle u'^2\rangle = I_{\langle u'^2\rangle} + II_{\langle u'^2\rangle} + III_{\langle u'^2\rangle} + IV_{\langle u'^2\rangle};\\ &I_{\langle u'^2\rangle} = -2\nu\langle \nabla u' \cdot \nabla u'\rangle, \quad II_{\langle u'^2\rangle} = 2\left\langle p'\frac{\partial u'}{\partial x}\right\rangle,\\ &III_{\langle u'^2\rangle} = \frac{\partial}{\partial z}\left(\nu\frac{\partial}{\partial z}(\langle u'^2\rangle) - \langle w'u'^2\rangle\right), \quad IV_{\langle u'^2\rangle} = -2\langle u'w'\rangle\frac{\partial}{\partial z}\overline{U}. \end{aligned}\right\} \tag{5.1}$$

The budget terms are normalized by the quantity $U(0)^3\alpha$. The normalized terms for $\langle u'^2\rangle$ are plotted in figure 25(*a*) for the strongly stratified case 2. The only source term is the shear production ($IV_{\langle u'^2\rangle}$). It has two peaks, located on either side of the model jet stream, in agreement with the graph of $\langle u'^2\rangle$ in figure 15. The energy produced is either dissipated or transferred to other components through ($I_{\langle u'^2\rangle}$) and ($II_{\langle u'^2\rangle}$) terms, respectively. The pressure term consists of two peaks directly opposite to the peaks of the production terms, transferring energy from the streamwise direction to the spanwise and vertical directions. The dissipation term has the largest values at the centre, and it decreases away from the centre. The transport term ($III_{\langle u'^2\rangle}$) moves energy from the peaks to the centre and a lesser amount to the outer edges of the jet.

The budget equation for the spanwise velocity is

$$\left.\begin{aligned} &\frac{\partial}{\partial t}\langle v'^2\rangle = I_{\langle v'^2\rangle} + II_{\langle v'^2\rangle} + III_{\langle v'^2\rangle} + IV_{\langle v'^2\rangle};\\ &I_{\langle v'^2\rangle} = -2\nu\langle \nabla v' \cdot \nabla v'\rangle, \quad II_{\langle v'^2\rangle} = 2\left\langle p'\frac{\partial v'}{\partial y}\right\rangle,\\ &III_{\langle v'^2\rangle} = \frac{\partial}{\partial z}\left(\nu\frac{\partial}{\partial z}(\langle v'^2\rangle) - \langle w'(v'^2)\rangle\right), \quad IV_{\langle v'^2\rangle} = -2\langle v'w'\rangle\frac{\partial}{\partial z}\overline{V}, \end{aligned}\right\} \tag{5.2}$$

which are shown in figure 25(*b*). The source is the pressure term ($II_{\langle v'^2\rangle}$) which transfers energy from the streamwise to the spanwise direction. The dissipation term

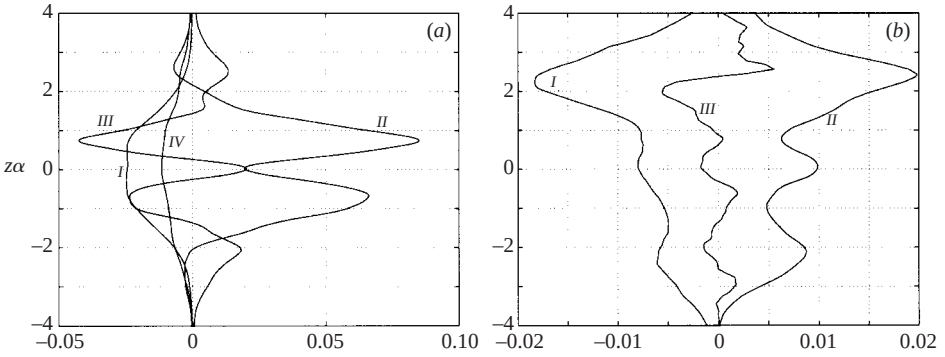

FIGURE 26. (*a*) The normalized horizontally averaged budgets in the equation for the vertical velocity variance for case 2. (*b*) The normalized budgets in the equation for temperature variance. Labels in the figures correspond to *I* – dissipation, *II* – pressure, *III* – transport, *IV* – buoyancy flux (in (*a*) only).

($I_{\langle v'^2\rangle}$), in contrast to the streamwise component, has two side peaks. The transport term ($III_{\langle v'^2\rangle}$) moves energy from each side to the centre and away from the jet. The shear production term $IV_{\langle v'^2\rangle}$ in the spanwise direction is small compared to the other terms.

The budget equation for the vertical velocity is

$$\left.\begin{aligned} &\frac{\partial}{\partial t}\langle w'^2\rangle = I_{\langle w'^2\rangle} + II_{\langle w'^2\rangle} + III_{\langle w'^2\rangle} + IV_{\langle w'^2\rangle};\\ &I_{\langle w'^2\rangle} = -2\nu\langle \nabla w' \cdot \nabla w'\rangle, \quad II_{\langle w'^2\rangle} = 2\left\langle p'\frac{\partial}{\partial z}w'\right\rangle,\\ &III_{\langle w'^2\rangle} = \frac{\partial}{\partial z}\left(\nu\frac{\partial}{\partial z}\langle w'^2\rangle - \langle w'^3\rangle - 2\langle p'w'\rangle\right), \quad IV_{\langle w'^2\rangle} = 2N\langle w'\vartheta'\rangle, \end{aligned}\right\} \tag{5.3}$$

which are shown in figure 26(*a*). The pressure redistribution term ($II_{\langle w'^2\rangle}$) extracts energy from the streamwise direction, and this energy is either dissipated ($I_{\langle w'^2\rangle}$) or converted to potential energy through the buoyancy term ($IV_{\langle w'^2\rangle}$). The dissipation term here has magnitude similar to that in the spanwise direction; but this term is now dominant at the centre. The transport term ($III_{\langle w'^2\rangle}$) plays a more significant role than in the spanwise direction, in that it transports energy from the jet shear layer area to the outer region (which may be responsible for the intermittent wave breaking activity seen in figures 13 and 14). The buoyancy term is negative and heat flux is thus down gradient (from hot to cold). No counter-gradient heat flux was observed from the equilibrium statistics (figure 20).

The budget equation for the temperature is

$$\left.\begin{aligned} &\frac{\partial}{\partial t}\langle \vartheta'^2\rangle = I_{\langle \vartheta'^2\rangle} + II_{\langle \vartheta'^2\rangle} + III_{\langle \vartheta'^2\rangle},\\ &I_{\langle \vartheta'^2\rangle} = -2\kappa\langle \nabla\vartheta' \cdot \nabla\vartheta'\rangle,\\ &II_{\langle \vartheta'^2\rangle} = -2\langle w'\vartheta'\rangle\left(NK^2 + \frac{\partial}{\partial z}\langle\vartheta\rangle\right) = -2\langle w'\vartheta'\rangle\frac{N_{eq}^2}{N},\\ &III_{\langle \vartheta'^2\rangle} = \frac{\partial}{\partial z}\left(\kappa\frac{\partial}{\partial z}\langle\vartheta'^2\rangle - \langle w'\vartheta'^2\rangle\right), \end{aligned}\right\} \tag{5.4}$$

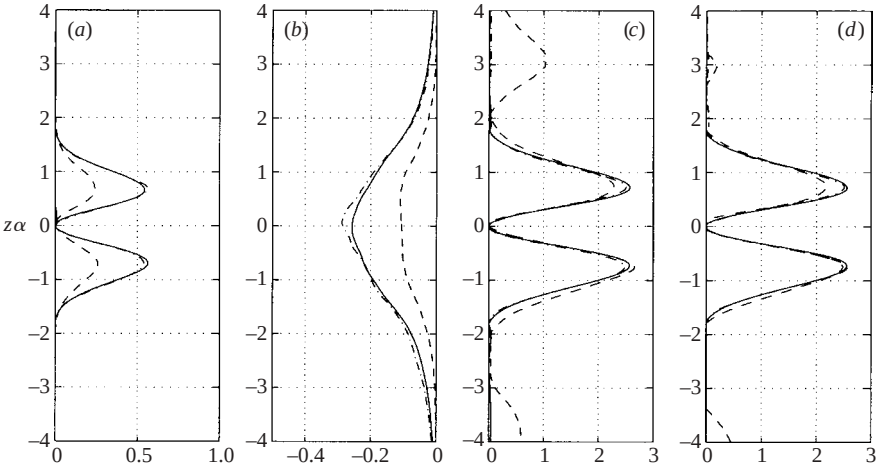

FIGURE 27. (*a*) Normalized shear production; (*b*) normalized dissipation; (*c*) shear production over dissipation and (*d*) growth parameter for cases 1 (solid), 2 (dash) and 3 (dash-dot). Curves for cases 1 and 3 are nearly identical.

which are shown in figure 26(*b*). The gradient production term ($II_{\langle\vartheta'^2\rangle}$) is the only source term. It has a peak at about $z\alpha \approx 2$. The dissipation term ($I_{\langle\vartheta'^2\rangle}$) has roughly the same shape as the production term but, of course, with the opposite sign. This may explain why counter-gradient fluxes are not observed in figure 26(*a*); temperature anomalies dissipate in the generation region, without producing restratification effects that would lead to counter-gradient fluxes. The transport term ($III_{\langle\vartheta'^2\rangle}$) is relatively small.

The normalized shear production ($IV_{\langle u'^2\rangle}$) in the streamwise direction for cases 1, 2 and 3 is shown in figure 27(*a*). Cases 1 and 3 have nearly identical shear production. Case 2, which is more stably stratified, has smaller shear production at each vertical level compared to cases 1 and 3. Thus, the normalized shear production decreases with increasing stratification in our flows. This is consistent with the conclusion in Holt *et al.* (1992) that stratification does not directly reduce the growth of q^2 (i.e. is not a kinetic energy sink), but it indirectly suppresses the shear production (see also Rohr *et al.* 1988). The normalized total dissipation ($I_{\langle u'^2\rangle} + I_{\langle v'^2\rangle} + I_{\langle w'^2\rangle}$) for the three cases is shown in figure 27(*b*). The dissipation for case 2 decreases following the decrease in production. The ratio of production to dissipation is shown in figure 27(*c*). The three curves nearly collapse into one, suggesting that production and dissipation maintain the same ratio regardless of stratification. However, the ratio changes with $z\alpha$ and peaks at the edges of the jet, where shearing is maximum, $z\alpha \approx 1$. Surrounding the jet, the production and dissipation are not at equilibrium and the transport must be taken into account. Another relevant quantity is the growth parameter F as defined in Holt *et al.* (1992):

$$F = \frac{\text{production} - \text{buoyancy}}{\text{dissipation}} = \frac{\left|IV_{\langle u'^2\rangle}\right| - \left|IV_{\langle w'^2\rangle}\right|}{\left|I_{\langle u'^2\rangle}\right| + \left|I_{\langle v'^2\rangle}\right| + \left|I_{\langle w'^2\rangle}\right|}. \tag{5.5}$$

The dependence of F on $z\alpha$ is shown in figure 27(*d*). It varies roughly between 0 and 2.5 depending on the vertical level. We note that F is roughly equal to unity in homogeneous simulations at a critical Richardson number, e.g. Holt *et al.* (1992), as well as in laboratory experiments, e.g. Strang & Fernando (2001). The departure from

unity in the present simulations suggests that the role of TKE transport is significant at some vertical levels.

6. Conclusions

Three-dimensional quasi-equilibrium dynamics of shear-stratified turbulence in a model tropospheric jet was studied using DNS. Within the jet core, the Richardson number is low, the Ozmidov scale is high compared to shear scales, the turbulent energy production peaks and the turbulence is sustained; the Ozmidov scale has nearly three decades of separation from the Kolmogorov scale. The Richardson number increases beyond the jet shear layers in such a way that the shear length scale exceeds the buoyancy scale, thus impeding sustained energy transfer to turbulence by the mean flow. The turbulence in this region is patchy, in agreement with the observation of Nastrom & Eaton (2001). Beyond the edges of the jet are regions with moderate Richardson number characterized by small Ozmidov-to-buoyancy-scale ratio, indicating the presence of stably stratified turbulence; the shear production rate therein is vanishingly small and the energy supply to this region occurs via propagating nonlinear gravity waves (the nonlinear transport term in the energy budget exceeds the pressure transport term). Our DNS further show that with decreasing background stratification, the regions of enhanced nonlinear wave activities separate away vertically from the levels of peak shear production. These findings are consistent with the observations made in atmospheric jet streams (Bedard *et al.* 1986; Dalaudier *et al.* 1994). This is also in agreement with the theoretical and numerical studies of Sutherland & Peltier (1993, 1995), although their studies dealt with two-dimensional decaying jets and excitation of internal waves by such jets. Theoretical analysis of stratified shear flows has further established that propagating wave modes are forced at the shear layers; this shear instability then supports wave radiation when the density stratification outside the shear layer is sufficiently large (Lott *et al.* 1992); this is borne out by the present simulations.

Our simulations were performed with lower Reynolds numbers than in the atmosphere. Nevertheless, certain important parameters of computed turbulent fields are not only in qualitative but also in quantitative agreement with observed geophysical flows. For example, computed ratios and variability of turbulent outer length scales (Ozmidov, buoyancy, shear and Ellison) are broadly consistent with the observational data presented in Bedard *et al.* (1986), Eaton & Nastrom (1998), Nastrom *et al.* (1986), Hunt *et al.* (1985) and Hebert *et al.* (1992). The ratios of outer length scales are found to be in agreement with observations. These ratios do not change appreciably with increasing Reynolds number and they saturate with increasing numerical resolution. This is demonstrated in figure 23(*b*) where the ratio L_e/L_b is plotted for cases 4, 5 and 6. Remarkably, the curves show little variation, and saturate with increased resolution; vertical resolution doubles from cases 4 and 5 (512 vertical levels) to case 6 (1024 vertical levels). This guarantees that our resolution of the outer scales is grid independent and physically significant.

Descriptions of non-homogeneous turbulence and especially turbulence closure models in stratospheric layers require parameterizations and scaling laws for the length scales. As there are a number of different natural length scales for non-uniformly stratified jets, it is not clear, without additional theoretical arguments, numerical or experimental data, which scales are appropriate for parameterization of multiple branches in the scaling of flux Richardson number with Ri_g and other turbulent quantities for non-uniformly stratified tropopausal turbulence generated by

jet streams (Joseph *et al.* 2003). Having established a rigorous method to realize and simulate non-homogeneous stratified shear flows in the vicinity of the tropopause and identified key dynamical processes at work through energy budgets and length-scale ratio computations, in our future work we will investigate the parameterizations for various turbulence statistics in the context of non-homogeneous tropopausal turbulence.

We would like to thank Professor J. C. R. Hunt and Dr O. Cote for the useful discussions. Drs J. C. McWilliams and R. Kerr have also given us valuable comments. The simulations were performed on the parallel supercomputer of the Advanced Computing Laboratory at Los Alamos National Laboratory (we wish to thank Dr R. C. Malone for this) and the ARL MSRC under the sponsorship of the DoD HPC Challenge Program. Preliminary results of this work were reported in the Conference in honor of Professor Leibovich held at Cornell University in 1999. This work is supported by the AFOSR Contract FG9620-99-1-0300 and the DoD HPC Challenge Program.

REFERENCES

Alisse, J. -R. & Sidi, C. 2000 Experimental probability density functions of small-scale fluctuations in the stably stratified atmosphere. *J. Fluid Mech.* **402**, 137–162.

Babin, A., Mahalov, A. & Nicolaenko, B. 1998 On nonlinear baroclinic waves and adjustment of pancake dynamics. *Theoret. Comput. Fluid Dyn.* **11**, 215–235.

Batchelor, G. K. 1953 *Theory of Homogeneous Turbulence*. Cambridge University Press.

Bedard, A. J. Jr., Canavero, F. & Einaudi, F. 1986 Atmospheric gravity waves and aircraft turbulence encounters. *J. Atmos. Sci.* **43**, 2838–2844.

Beland, R. 1993 Propagation through atmospheric optical turbulence. In *Atmospheric Propagation of Radiation* (ed. F. G. Smith), pp. 157–232. SPIE Optical Engng Press, Washington.

Bell, J. H. & Mehta, R. D. 1990 Development of a two-stream mixing layer from tripped and untripped boundary layers. *AIAA J.* **28**, 2034–2042.

Carnevale, G. F., Briscoline, M. & Orlandi, P. 2001 Buoyancy to inertial range transition in forced stratified turbulence. *J. Fluid Mech.* **427**, 205–239.

Cote, O. R., Roadcap, J. R., Wroblewski, D. E., Dobosy, R. J., & Crawford, T. L. 2003 Aircraft measurements of turbulence: length scales, spectra, budgets, and the prediction problem. *12th Symp. Met. Observations and Instrumentation, 83rd AMS Meeting, Feb. 2003, Long Beach, CA.*

Cullen, M. J. P. 2002 New mathematical developments in atmosphere and ocean dynamics, and their application to computer simulations. In *Large-scale Atmosphere-Ocean Dynamics I, Analytical Methods and Numerical Models*, pp. 202–287. Cambridge University Press.

Dalaudier, F., Sidi, C., Crochet, M. & Vernin, J. 1994 Direct evidence of "sheets" in the atmospheric temperature field. *J. Atmos. Sci.* **51**, 237–248.

De Silva, I. P. D. & Fernando, H. J. S. 1992 Some aspects of mixing in a stratified turbulent patch. *J. Fluid Mech.* **240**, 601–625.

Eaton, F. D. & Nastrom, G. D. 1998 Preliminary estimates of the vertical profiles of inner and outer scales from White Sands Missile Range, New Mexico, VHF radar observations. *Radio Sci.* **33**, 895–903.

Fernando, H. J. S. 2002 Turbulence in stratified fluids. In *Environmental Stratified Flows* (ed. R. Grimshaw), pp. 163–193. Kluwer.

Fernando, H. J. S. & Hunt, J. C. R. 1996 Some aspects of turbulence and mixing in stably stratified layers. *Dyn. Atmos. Oceans* **23**, 35–62.

Fornberg, B. 1996 *A Practical Guide to Pseudospectral Methods*. Cambridge University Press.

Galmiche, M., Thual, O. & Bonneton, P. 2002 Direct numerical simulation of turbulence-mean field interactions in a stably-stratified fluid. *J. Fluid Mech.* **455**, 213–242.

Gargett, A., Osborne, T. R. & Nasmyth, P. W. 1984 Local isotropy and the decay of turbulence in a stably stratified fluid. *J. Fluid Mech.* **144**, 231–280.

Gerz, T., Schumann, U. & Elghobashi, S. E. 1989 Direct numerical simulation of stratified homogeneous turbulent shear flow. *J. Fluid Mech.* **200**, 563–594.

Grell, G. A., Dudhia, J. & Stauffer, D. R. 1995 A description of the fifth-generation Penn State/NCAR mesoscale model (MM5). NCAR/TN-398+STR, 122 pp.

Hebert, D., Moum, J. N., Paulson, C. A. & Caldwell, D. R. 1992 Turbulence and internal waves in the equator. Part II: details of a single event. *J. Phys. Oceanogr.* **22**, 1346–1356.

Herring, J. R. & Metais, O. 1989 Numerical experiments in forced stably stratified turbulence. *J. Fluid Mech.* **202**, 97–115.

Holt, S. E., Koseff, J. R. & Ferziger, J. H. 1992 A numerical study of the evolution and structure of homogeneous stably stratified sheared turbulence. *J. Fluid Mech.* **237**, 499–539.

Hunt, J. C. R. & Galmiche, M. 2001 Dynamics of layers in geophysical flows. In *Fluid Mechanics and the Environment: Dynamical Approaches* (ed. J. L. Lumley), Lecture Notes in Physics, vol. 566, pp. 121–151. Springer.

Hunt, J. C. R., Kaimal, J. C. & Gaynor, J. E. 1985 Some observations of turbulence structure in stable layers. *Q. J. R. Met. Soc.* **111**, 793–815.

Itsweire, E. C., Koseff, J. R., Briggs, D. A. & Ferziger, J. H. 1993 Turbulence in stratified shear flows: implications for interpreting shear-induced mixing in the ocean. *J. Phys. Oceanogr.* **23**, 1508–1522.

Jacobitz, F. G., Sarkar, S. & Van Atta, C. W. 1997 Direct numerical simulations of the turbulence evolution in a uniformly sheared and stably stratified flow. *J. Fluid Mech.* **342**, 231–261.

Joseph, B., Mahalov, A., Nicolaenko, B. & Tse, K. L. 2003 High resolution DNS of jet stream generated tropopausal turbulence. *Geophys. Res. Lett.* **30**, 1525–1530.

Kaltenbach, H. J., Gerz, T. & Schumann, U. 1994 Large-eddy simulation of homogeneous turbulence and diffusion in stably stratified shear flow. *J. Fluid Mech.* **280**, 1–40.

Keyser, D. & Shapiro, M. A. 1985 A review of the structure and dynamics of upper-level frontal zones. *Mont. Weath. Rev.* **114**, 452–499.

Lott, F., Kelder, H. & Teitelbaum, H. 1992 A transition from Kelvin-Helmholtz instabilities to propagating wave instabilities. *Phys. Fluids* A **4**, 1990–1997.

Mahalov, A., Nicolaenko, B. & Zhou, Y. 1998 Energy spectra of strongly stratified and rotating turbulence. *Phys. Rev.* E **57**, 6187–6190.

Moum, J. N. 1996 Energy-containing scales of turbulence in the ocean thermocline. *J. Geophys. Res.* **101**, 14095–14109.

Nastrom, G. D. & Eaton, F. D. 1997 Turbulence eddy dissipation rates from radar observations at 5-20 km at White Sands Missile Range, New Mexico. *J. Geophys. Res.* **102**, 19495–19505.

Nastrom, G. D. & Eaton, F. D. 2001 Persistent layers of enhanced C_N^2 in the lower stratosphere from VHF radar observation. *Radio Sci.* **36**, 137–149.

Nastrom, G. D. & Gage, K. S. 1985 A climatology of atmospheric wavenumber spectra of wind and temperature observed by commercial aircraft. *J. Atmos. Sci.* **42**, 950–960.

Nastrom, G. D., Gage, K. S. & Ecklund, W. L. 1986 Variability of turbulence, 4-20km, in Colorado and Alaska from MST radar observations. *J. Geophys. Res.* **91**, 6722–6734.

Pardyjak, E. I., Monti, P. & Fernando, H. J. S. 2002 Flux Richardson number measurements in stable atmospheric shear flows. *J. Fluid Mech.* **459**, 307–316.

Peltier, W. R. & Caulfield, C. P. 2003 Mixing efficiency in stratified shear flows. *Annu. Rev. Fluid Mech.* **35**, 135–168.

Phillips, O. M. 1972 Turbulence in a strongly stratified fluid – is it unstable? *Deep Sea Res.* **19**, 79–81.

Phillips, O. M. 1991 The Kolmogorov spectrum and its oceanic cousins: a review. *Proc. R. Soc. Lond.* A **434**, 125–138.

Pope, S. B. 2000 *Turbulent Flows*. Cambridge University Press.

Riley, J. J. 2001 Dynamics of turbulence strongly influenced by buoyancy. *Environmental Fluid Dynamics Seminar, Arizona State University*.

Riley, J. J., Metcalfe, R. W. & Weissman, M. A. 1981 Direct numerical simulations of homogeneous turbulence in density stratified fluids. *Proc. AIP Conf. on Nonlinear Properties of Internal Waves*, vol. 76, pp. 79–112.

Rogers, M. M. & Moser, R. D. 1993 Direct simulation of a self-similar turbulent mixing layer. *Phys. Fluids* **6**, 903–923.

Rohr, J. J., Itsweire, E. C., Helland, K. N. & Van Atta, C. W. 1988 Growth and decay of turbulence in a stably stratified shear flow. *J. Fluid Mech.* **195**, 77–111.

Schumann, U. 1996 Direct and large eddy simulations of stratified homogeneous shear flows. *Dyn. Atmos. Oceans* **23**, 81–98.

Schumann, U. & Gerz, T. 1995 Turbulent mixing in stably stratified shear flows. *J. Appl. Met.* **34**, 33–48.

Shih, L. H., Koseff, J. R., Ferziger, J. H. & Rehmann, C. R. 2000 Scaling and parametrization of stratified homogeneous turbulent shear flow. *J. Fluid Mech.* **412**, 1–20.

Smyth, W. D. & Moum, J. N. 2000 Anisotropy of turbulence in stably stratified mixing layers. *Phys. Fluids.* **12**, 6, 1343–1362.

Smyth, W. D. & Moum, J. N. 2002 Shear instability and gravity wave saturation in an asymmetrically stratified jet. *Dyn. Atmos. Oceans* **35**, 265–294.

Stewart, R. W. 1969 Turbulence and waves in a stratified atmosphere. *Radio Sci.* **4**, 1269–1278.

Strang, E. J. & Fernando, H. J. S. 2001 Entrainment and mixing in stratified shear flows. *J. Fluid Mech.* **428**, 349–386.

Stull, R. B. 1988 *Introduction to Boundary Layer Meteorology*. Kluwer.

Sutherland, B. R. & Linden, P. F. 1998 Internal wave excitation from stratified flow over a thin barrier. *J. Fluid Mech.* **377**, 223–252.

Sutherland, B. R. & Peltier, W. R. 1993 Turbulence transition and internal wave generation in density stratified jets. *Phys. Fluids.* **6**, 1267–1284.

Sutherland, B. R. & Peltier, W. R. 1995 Internal gravity wave emission into the middle atmosphere. *J. Atmos. Sci.* **52**, 3214–3234.

Thorpe, S. A. 1987 Transitional phenomena and the development of turbulence in stratified fluids: a review. *J. Geophys. Res.* **92**, 5231–5248.

Tse, K. L., Mahalov, A., Nicolaenko, B. & Fernando, H. J. S. 2001 A spectral domain decomposition method and its application to simulations of shear-stratified turbulence. In *Fluid Mechanics and the Environment: Dynamical Approaches* (ed. J. L. Lumley), Lecture Notes in Physics, vol. 566, pp. 353–378. Springer.

Vinnichenko, N. K. 1980 *Turbulence in the Free Atmosphere*, 2nd Edn. New York: Consultant's Bureau.

Webster, C. A. G. 1964 An experimental study of turbulence in a density-stratified shear flow. *J. Fluid Mech.* **19**, 221–245.

Webster, D. R. & Liu, Y. 2001 Velocity measurements of turbulence collapse in a linearly stratified jet. *Exps. Fluids* **54**, 394–400.